The Astrophysical Journal, 793:96 (18pp), 2014 October 1 doi:10.1088/0004-637X/793/2/96

A CALIBRATION OF THE STELLAR MASS FUNDAMENTAL PLANE AT $z \sim 0.5$ USING THE MICRO-LENSING-INDUCED FLUX RATIO ANOMALIES OF MACRO-LENSED QUASARS*,†,‡

Paul L. Schechter[1,2,3], David Pooley[4,5], Jeffrey A. Blackburne[6], and Joachim Wambsganss[7,8]
[1] MIT Kavli Institute for Astrophysics and Space Research, Cambridge, MA 02139, USA
[2] Department of Physics, Massachusetts Institute of Technology, 77 Massachusetts Avenue, Cambridge, MA 02139, USA
[3] Department of Astronomy, Williams College, Hopkins Hall, 880 Main Street, Williamstown, MA 01267, USA
[4] Sam Houston State University, Huntsville, TX 77341, USA
[5] Eureka Scientific, Inc., 2452 Delmer Street, Suite 100, Oakland, CA 94602, USA
[6] Areté Associates, Northridge, CA 91324, USA
[7] Zentrum für Astronomie der Universität Heidelberg, Heidelberg D-69120, Germany
[8] Pauli Center for Theoretical Studies, ETH Zürich
Received 2014 April 30; accepted 2014 July 23; published 2014 September 11

ABSTRACT

We measure the stellar mass surface densities of early-type galaxies by observing the micro-lensing of macro-lensed quasars caused by individual stars, including stellar remnants, brown dwarfs, and red dwarfs too faint to produce photometric or spectroscopic signatures. Instead of observing multiple micro-lensing events in a single system, we combine single-epoch X-ray snapshots of 10 quadruple systems, and compare the measured relative magnifications for the images with those computed from macro-models. We use these to normalize a stellar mass fundamental plane constructed using a Salpeter initial mass function with a low-mass cutoff of 0.1 $M_\odot$ and treat the zeropoint of the surface mass density as a free parameter. Our method measures the *graininess* of the gravitational potential produced by individual stars, in contrast to methods that decompose a smooth total gravitational potential into two smooth components, one stellar and one dark. We find the median likelihood value for the normalization factor $\mathcal{F}$ by which the Salpeter stellar masses must be multiplied is 1.23, with a one sigma confidence range, dominated by small number statistics, of $0.77 < \mathcal{F} < 2.10$.

Key words: galaxies: stellar content – gravitational lensing: micro – gravitational lensing: strong

1. INTRODUCTION

1.1. Stellar Masses from Micro-lensing

So-called stellar masses for early-type galaxies are almost always determined by one of two methods: either they are estimated from spectra (sometimes only broadband colors) or they are deduced by subtracting the contribution of an assumed dark matter component from a combined mass inferred from kinematic (and sometimes macro-lensing) measurements. The two methods, with their many variants, are described at length in the review by Courteau et al. (2014).

Both methods have shortcomings. Spectral methods suffer from the fact that lower main sequence stars, substellar objects, and stellar remnants contribute negligibly to the observed light and therefore cannot be detected in spectra. Such determinations must therefore rely on some assumed shape for the stellar mass function. To quote from a frequently cited example of these efforts (Kauffmann et al. 2003, p. 48). "All of our derived parameters are tied to a specific choice of IMF [initial mass function]. Changing the IMF would scale the stellar mass estimates by a fixed factor. For example, changing from a Kroupa (2001) to a Salpeter IMF with a cutoff at 0.1 $M_\odot$ would result in a factor of two increase in the stellar mass."

Dark matter subtraction techniques are vulnerable to mistaken assumptions about the density profile of the dark matter and to mistaken assumptions about the constancy or non-constancy of the mass-to-light ratio of the stellar component. A recent paper by Cappellari et al. (2012) illustrates the effects of varying assumptions about the shapes of dark matter halos.

In this paper we use a third method: determining the stellar mass surface density of an early-type galaxy from brightness fluctuations of the four images of a background quasar that is both multiply imaged ("macro-lensed") by the galaxy and micro-lensed by the individual stars in that galaxy (Schechter & Wambsganss 2004; Kochanek 2004). This method, in contrast to spectral methods, is sensitive to stellar mass near and below the hydrogen burning limit, as well as to mass in stellar remnants. Also, where dark matter subtraction methods make assumptions about the dark matter profiles, the gravitational micro-lensing technique makes only an assumption about the combined gravitational potential, one that has been subjected to extensive observational verification.

Micro-lensing produces flux ratio anomalies of the sort described by Schechter & Wambsganss (2002). Ideally one would observe a single system long enough to see a great many fluctuations and infer an accurate stellar surface density. But the timescale for micro-lensing variations is of the order of 10 yr for a lens at redshift $z \sim 0.5$ (Mosquera & Kochanek 2011), and observations of even four quasar images at a single epoch give only broad constraints on the mass surface density via the deviation of the observed flux ratios from those predicted by a macro-model. So instead we observe a number of systems at a single epoch and combine results.

Such a measurement is no different, in principle, from the measurement of the density of massive compact halo objects in

* The scientific results reported in this article are based to a significant degree on observations made with the *Chandra X-ray Observatory* and published previously in cited articles.
† This paper includes data gathered with the 6.5 m Magellan telescopes located at Las Campanas Observatory, Chile.
‡ Based in part on observations made with the NASA/ESA *Hubble Space Telescope*, obtained at the Space Telescope Science Institute, which is operated by the Association of Universities for Research in Astronomy, Inc., under NASA contract NAS5-26555. These observations are associated with program GO-9854.

the Milky way via micro-lensing measurements of stars in the Magellanic Clouds (Paczyński 1986b), though it differs in the nature of the source that is lensed and in the very much higher optical depth (Paczyński 1986a; Witt et al. 1995) along the lines of sight to multiply imaged quasars.

There is as yet no theory that predicts in closed form the statistics of such light curves as a function of point mass density and external shear, at least not at the optical depths we consider. One must therefore carry out simulations for each case of interest, using the ray shooting technique pioneered by Kayser et al. (1986) and Schneider & Weiss (1987), and refined by Wambsganss (1990).

It is the peculiar property of such micro-lensing that the instantaneous magnification probability distribution is determined almost entirely by the surface mass density of micro-lenses, with a dependence upon the distribution of masses that is so weak that only with elaborately contrived simulations can it be observed at all (Schechter et al. 2004).

1.2. The Stellar Mass Fundamental Plane

The combination of a set of results from multiple quasars is non-trivial for several reasons: (1) the lens galaxies do not all have the same linear sizes and stellar mass surface densities, (2) the quasar lines of sight do not all sample the same projected distance from the lens, and (3) the lenses lie at different redshifts. Ideally our combined result would give the mass surface density for an early-type galaxy of a fiducial size at a fiducial radius and a fiducial redshift.

The stellar mass fundamental plane (Hyde & Bernardi 2009) can be used to scale measured stellar surface densities to a common velocity dispersion (which we take to indicate the size of the dark matter halo in which the lensing galaxy is embedded) and projected distance, as a fraction of the measured effective radius.

Alternatively, one may use the stellar mass fundamental plane to "predict" the stellar mass surface density at a given projected radius for a galaxy with a specified velocity dispersion and effective radius. Multiplying these predictions by an adjustable constant and minimizing residuals between the measured and predicted stellar mass surface densities allows one to recalibrate the stellar mass fundamental plane. If the correct initial mass function (IMF) has been used in deriving the adopted stellar mass fundamental plane, the adjustable parameter, $\mathcal{F}$, will be unity.

In the present work we construct two stellar mass fundamental planes, one derived from measurements by Auger et al. (2010) for the Sloan Lens Advanced Camera for Surveys (hereafter referred to as SLACS) sample at $z \sim 0.2$ and another derived from measurements by Sonnenfeld et al. (2013) for the Strong Lensing Legacy Survey (hereafter referred to as SL2S) sample at $z \sim 0.5$. Both groups of authors use Salpeter (1955) IMFs to calculate stellar mass.[9] We use both samples to constrain the orientation of the fundamental plane, but then fit them separately to allow for possible evolution with redshift.

1.3. Previous Investigations

Past efforts to ascertain stellar (or alternatively dark) mass contributions to galaxy masses based on micro-lensing have been carried out in large part by two groups—one that builds upon the work of Kochanek (2004), and another that builds upon the work of Schechter & Wambsganss (2004). Other efforts include those of Mediavilla et al. (2009), Bate et al. (2011), and Oguri et al. (2014), the last of which uses the stellar mass fraction derived by the present authors (Pooley et al. 2012) as a constraint in what is otherwise a decomposition into two smooth components, one stellar and one dark.

The present paper produces results that are somewhat less uncertain, and somewhat more robust, but differs primarily in that our central goal is a calibration of the conversion of observed light to stellar mass rather than determining a dark or stellar mass fraction.

1.4. Quasars as Point Sources

The analysis of optical flux ratio anomalies for a set of quadruply lensed quasars by Schechter & Wambsganss (2004) was inconclusive. Including the case of SDSS J0924+0219, they found an implausibly low-mass fraction. Excluding it gave a double-peaked likelihood function. They were able to produce a single peak by making the *ad hoc* assumption that in every case 50% of the quasar light came from a point source and 50% of the light came from a source too extended to be micro-lensed.

Chandra X-ray Observatory observations of those same quadruply lensed quasars indicate that finite size effects may indeed have been responsible for Schechter & Wambsganss' (2004) failure to extract a clean signal from the optical flux ratios. Pooley et al. (2007) found for a sample of 10 lensed systems that the X-ray deviations from models with smooth potentials, as measured in magnitudes, were a factor of two larger than the optical deviations. They argue that the optical emission comes from a larger region comparable in size to the Einstein rings of the micro-lensing stars.

While the size of a quasar's optical emission region relative to that of stellar Einstein rings may be of interest in its own right, for the present purpose it is yet another free parameter and a major nuisance. Fortunately, the X-ray emission appears to emanate from a very compact, more nearly pointlike region. In the present paper we use these X-ray observations to determine stellar mass surface densities.

1.5. Smoothly Distributed Dark Matter

The micro-lensing magnification distribution expected at the position of one of our quasar images depends not only on the stellar mass density, but also on the tidal shear due to the galaxy and the magnification produced by the smooth dark matter density at that position. We use an isothermal model for the potential produced by the combined gravity of the stellar and dark matter components of our lensing galaxies, consistent with results from the SLACS survey (Gavazzi et al. 2007; Auger et al. 2010), the SL2S survey (Ruff et al. 2011), and a combined analysis of the SLACS and BELLS samples (Bolton et al. 2012).

1.6. Outline

In Section 2 we construct stellar-mass fundamental planes using the SLACS data of Auger et al. (2010) and the SL2S data of Sonnenfeld et al. (2013) for subsequent use in analyzing quasar micro-lensing.

In Section 3 we assemble the observational data needed for our analysis. These include positions and effective radii for the lensing galaxies, and positions and X-ray fluxes for the lensed quasar images.

[9] A low mass cutoff must be applied to the Salpeter (1955) IMF to keep the integrated mass from diverging. Auger et al. (2010) and Sonnenfeld et al. (2013) used a low mass cutoff of 0.10 $M_\odot$ (T. Treu 2014, private communication).

In Section 4 we present macro-lensing models for the lensed quasars, with particular emphasis on the total mass surface densities and shears at the quasar image positions.

In Section 5 we describe the suite of ray tracing simulations used in our likelihood analysis and our scheme for interpolating across them.

In Section 6 we present the details of our likelihood analysis.

In Section 7 we carry out that likelihood analysis and derive a re-calibration factor $\mathcal{F}$ for the SL2S stellar-mass fundamental plane. We then examine and discuss possible sources of systematic errors: our choice of models for the macro-lensing potential, our implicit prior on the unlensed x-ray fluxes of the lensed quasars, our method of analysis, systematic errors in the measurement of effective radii, and the sensitivity of our combined results to the results for the individual lensed systems.

In Section 8 we discuss our result in the context of other measurements.

In Section 9 we summarize our results and describe avenues for further refinement.

2. THE STELLAR MASS FUNDAMENTAL PLANE (AND LINE)

2.1. Basic Idea

The stellar mass fundamental plane (Hyde & Bernardi 2009) differs from the conventional fundamental plane (Djorgovski & Davis 1987) in that stellar surface mass density replaces stellar surface brightness as one of the three "observables" measured for elliptical or early-type galaxies. In either case the galaxies lie very close to a two-dimensional planar surface in the three-dimensional space spanned by the logarithms of the observables. For a given stellar mass fundamental plane, one might expect different (parallel) conventional fundamental planes for populations of different ages and metallicities. Observations of the galaxies with several filters would permit one to combine galaxies of different ages and metallicities into a single stellar mass fundamental plane. But this can be accomplished only by making assumptions about the IMF, since the stars that constitute the bulk of the mass contribute very little starlight.

Hyde and Bernardi cast their fundamental plane as a "prediction" of the effective radius r_e of an elliptical galaxy, assumed to follow a de Vaucouleurs (1948) surface brightness profile, given measurements of the average stellar surface mass density Σ_e interior to the effective radius and the stellar velocity dispersion, σ,

$$\log r_e = \alpha \log \sigma + \beta \log \Sigma_e + \gamma. \quad (1)$$

Observed values of the effective radius (the geometric mean of the semi-major and semi-minor axes) are compared with the predictions obtained with trial values of the coefficients, which are then adjusted to minimize the scatter between the observations and predictions.

For the present purposes we want a fundamental plane that "predicts" stellar surface mass densities as a function of effective radius and velocity dispersion,

$$\log \Sigma_e = a \log \sigma + b \log r_e + c. \quad (2)$$

We use the predicted surface mass densities to calculate the effects of micro-lensing at the four quasar image positions, and then adjust the constant c to maximize the likelihood of the observed fluxes based on the micro-lensing predictions. This is the sense in which we re-calibrate the stellar mass fundamental plane. We start with a fundamental plane computed from multi-color observations and adjust the stellar mass zeropoint to maximize the likelihood of the observed flux ratio anomalies.

2.2. Einstein Ring Radius as a Proxy for Stellar Velocity Dispersion

The use of the stellar mass fundamental plane to estimate stellar mass surface densities is rendered more challenging by the fact that our lensing galaxies are crowded by four bright quasar images, making it either difficult or impossible to measure stellar velocity dispersions for many of our lensing galaxies.[10] Fortunately, lensing galaxies are characterized by an Einstein ring radius that has a straightforward relation to the stellar velocity dispersion. We follow Kochanek et al. (2000) in constructing a stellar mass fundamental plane that employs these Einstein ring radii, converted to equivalent stellar velocity dispersions, and refer to them as "proxy" dispersions.

The potentials of early-type elliptical galaxies are very nearly isothermal (e.g., Auger et al. 2010), and for an isothermal sphere the isotropic stellar velocity dispersion can be read directly from the radius of the Einstein ring, $\theta_{\rm Ein}$, measured in radians,

$$\sigma_{\rm prox} = c\sqrt{\frac{\theta_{\rm Ein}}{4\pi}\frac{D_{LS}}{D_{OS}}}, \quad (3)$$

where D_{OS} and D_{LS} are the angular diameter distances from the observer to the source and from the lens to the source, respectively (Narayan & Bartelmann 1996). The radius of the Einstein ring, $\theta_{\rm Ein}$, is a direct output of our lens modeling described in Section 4 below.

The stars in the lensing galaxy may not have isotropic orbits. In that case, even though the potential might be that of an isothermal sphere, stellar velocity dispersions will depend upon the aperture used to measure them. By contrast, the Einstein ring radius suffers from no such shortcoming. Finding virtue in necessity, we use the Einstein ring radius as a proxy for stellar velocity dispersion in our construction of a stellar mass fundamental plane.

2.3. A Stellar Mass Fundamental Plane at $z \sim 0.2$

We use the data of Auger et al. (2010) for systems of emission line galaxies lensed by foreground early-type galaxies at a mean redshift of 0.2 to compute a stellar mass fundamental plane. Auger et al. give effective radii r_e measured in kiloparsecs computed at in the rest band of the V filter, and total stellar masses M^* based on two different assumed IMFs, Salpeter (1955), with a cutoff of 0.1 $M_\odot$, and Chabrier (2003), for 51 systems.[11] Treu et al. (2010) give Einstein ring radii computed from their singular isothermal ellipsoid lens models and expressed as proxy velocity dispersions for the same sample. As a starting point, we use these data to calculate a Salpeter stellar mass fundamental plane.

We divide our measured proxy dispersions and effective radii by typical values, 266 km s^{-1} and 6.17 kpc, respectively, so as to reduce (but not completely eliminate) the covariances between the derived coefficients,

$$\log \Sigma_e = a \log\left(\frac{\sigma_{\rm prox}}{266\ {\rm km\ s^{-1}}}\right) + b \log\left(\frac{r_e}{6.17\ {\rm kpc}}\right) + c. \quad (4)$$

[10] Despite this observational challenge, PG 1115+080, HE 0435−1223, RX J1131−1231, and RX J0911+0551 do have measured velocity dispersions.

[11] Following Auger et al., we adopt an $(h, \Omega_m, \Omega_\Lambda) = (0.7, 0.3, 0.7)$ cosmology.

Table 1
Stellar Mass Fundamental Plane Coefficients

$\log \Sigma_e = a \log(\sigma_{\rm prox}/266\ {\rm km\ s^{-1}}) + b \log(r_e/6.17\ {\rm kpc}) + c$					
Sample	a	b	c	r_{ab}	rms
SLACS[a]	0.767	−1.140	9.219		0.094
	±0.219	±0.086	±0.014	−0.622	
SLACS	1.590	−1.371	9.216		0.076
	±0.300	±0.100	±0.012	−0.796	
SL2S	1.934	−1.701	9.225		0.145
	±0.557	±0.166	±0.032	−0.538	
SLACS[b]	≡1.748	≡−1.453	9.220		0.077
	±0.260	±0.085	±0.011	−0.758	
SL2S[b]	≡1.748	≡−1.453	9.170		0.154
	±0.260	±0.085	±0.033	−0.758	

Notes.
[a] Uses stellar velocity dispersion σ rather than $\sigma_{\rm prox}$.
[b] a and b coefficients and errors are values for combined SLACS+SL2S sample.

The coefficients a, b, and c are given in Table 1, as is the r_{ab} correlation coefficient.

2.4. Stellar Mass Fundamental Plane Using Stellar Velocity Dispersions

We are driven to use Einstein ring radius as a proxy for stellar velocity dispersion because the light from our quasars overwhelms that of the lensing galaxies. But as Auger et al. (2010) are working with fainter lensed background galaxies, they *have* been able to measure stellar velocity dispersions, and their data may be used to calculate a proper stellar mass fundamental plane for the sake of comparison. The results are also given in Table 1.

The a and b coefficients for the stellar velocity dispersion fundamental plane are only marginally consistent with those obtained for the proxy dispersion fundamental plane, but the range of dispersions in our sample is relatively small. As the stellar velocity dispersions are slightly larger than the Einstein ring proxies, the zeropoint c is correspondingly smaller.

Also shown in Table 1 is the rms scatter in the logarithm of the surface mass density. It is considerably smaller, by a factor of 1.5, when one uses the proxy dispersion rather than the stellar dispersion. The most likely cause is measurement errors in the stellar dispersions, which are of order 10%. By contrast, Einstein ring radii are accurate to 1%.

It might also be the case that *both* the stellar velocity dispersion *and* the Einstein ring radius are stand-ins for some third quantity which gives a yet tighter fundamental plane. If that third quantity were the size (or mass or energy per unit mass) of the halo, one might expect the radius of the Einstein ring to represent it more faithfully than the stellar velocity dispersion, as it is less influenced by the stellar mass density at the center of the galaxy.

2.5. A Stellar Mass Fundamental Plane at $z \sim 0.5$

The data presented by Sonnenfeld et al. (2013) for lenses found in the SL2S may also be used to construct a stellar mass fundamental plane. While only 21 of their systems have complete data, the median redshift for their sample, 0.494, is much closer to the median for the lens systems used here. The sample was subject to different selection effects from that of Auger et al. (2010), but a common method for stellar mass estimation was used for both samples. A different scheme was used for measuring effective radii but they have also used singular isothermal ellipsoids to model their lenses and derive proxy velocity dispersions.

The coefficients derived for the SL2S sample are consistent with those derived for the SLACS sample but roughly a factor of three more uncertain. The scatter between the predicted and observed surface mass densities is higher for SL2S than it was for SLACS and, by contrast, no better for the proxy velocity dispersions than for the actual measured stellar velocity dispersions.

2.6. The Orientation of the Stellar Mass Fundamental Plane

So as to better compare the surface mass density at different redshifts, we wish to adopt a single orientation for the fundamental plane and fit that to both the SLACS and the SL2S. We have combined velocity dispersion and effective radius coefficients for the SLACS and SL2S samples using the a and b coefficients and uncertainties given in Table 1, to produce a and b coefficients for the combined sample. These are also given in Table 1.

2.7. Possible Differences between $z \sim 0.2$ and $z \sim 0.5$

We obtained new values for the stellar surface mass density coefficients for the SLACS and SL2S samples fixing the a and b coefficients at the common value. These are too are given in Table 1.

We see that stellar mass surface density at fixed velocity dispersion and effective radius for the SLACS sample is marginally higher, by roughly 11%, than for the SL2S. While the difference might be due to different selection criteria for the two samples, or to the different techniques used to extract effective radii, it might also be due to evolution in the fundamental plane. We therefore take the common orientation SL2S stellar mass fundamental plane as our primary predictor of the surface mass density along the lines of sight to our quasar images.

We note that Bezanson et al. (2013) see little or no evidence for evolution in the conventional stellar mass fundamental plane.

2.8. Systematic Errors in Effective Radii

Our stellar mass fundamental plane is only as good as the effective radius measurements, the velocity dispersion measurements (or their proxies), and the stellar mass estimates (derived from stellar colors) used to construct it. We have framed our effort as an attempt to calibrate the SLACS and SL2S stellar masses. But if there were a systematic error in the SLACS or SL2S effective radii, one might expect a corresponding systematic error in that calibration.

The situation is complicated by the fact that the effective radius measurements and the stellar mass surface density measurements are correlated. Unless the lines along which these quantities are correlated lie within the error-free stellar mass fundamental plane, the orientation of the derived plane will deviate systematically from the error-free orientation.

2.9. A Fundamental Line for Early-type Galaxies

One can construct a "fundamental line" for either of our samples by fitting separately for effective radius as function of velocity dispersion and stellar surface mass density as a function of velocity dispersion. Together these two relations give a line in the three-dimensional space of observables.[12] Both the effective

[12] Nair et al. (2011) describe a related fundamental line in the two-dimensional space spanned by effective radius and luminosity. Insofar as stellar mass and luminosity are strongly correlated, their fundamental line is a projection of the present one.

Table 2
Stellar Mass Fundamental Line Coefficients

$\log\Sigma_e = A\log(\sigma_{\rm prox}/265\ {\rm km\ s^{-1}}) + C$ $\log r_e = D\log(\sigma_{\rm prox}/265\ {\rm km\ s^{-1}}) + E$				
Sample	A	C	D	E
SLACS	−1.702	9.156	2.401	0.832
	±0.401	±0.024	±0.261	0.016

radii and the stellar surface mass densities scatter about their respective mean relations, but that scatter is strongly correlated, so that the galaxies fan out from the line into a plane.

Keeping that correlated scatter in mind, the relations

$$\log\Sigma_e = A\log\left(\frac{\sigma_{\rm prox}}{265\ {\rm km\ s^{-1}}}\right) + C \quad \text{and} \tag{5}$$

$$\log r_e = D\log\left(\frac{\sigma_{\rm prox}}{265\ {\rm km\ s^{-1}}}\right) + E, \tag{6}$$

can be used to look for possible systematic errors in the effective radii measured for the galaxies lensing our quasars, and to corroborate the result we obtain with the stellar mass fundamental plane. The denominator within the parenthesis is the sample logarithmic mean for the proxy velocity dispersion.

As we intend to use this only as a check on our fundamental plane results, we present in Table 2 only results for fits to the SLACS data. The uncertainties in the coefficients derived for the smaller SL2S sample render it less useful for our purposes.

3. DATA FOR LENSED QUASARS AND LENSING GALAXIES

3.1. Choice of Sample

Our sample of 10 multiply imaged quasars is a subset of the 15 systems considered by Blackburne et al. (2011).

The system Q2237+030 was eliminated because the half-light radius of the lensing galaxy (at $z = 0.04$) is very much larger than the Einstein ring radius, and the system appears to be a barred galaxy. Not coincidentally, it is the system that is best suited to a multi-epoch analysis, and has been analyzed by Kochanek (2004).

The system WFI J2026−4536 was eliminated because the redshift of the lensing galaxy has not been measured.

Two more systems, HE 1113−0641 and H1413+117, were eliminated because the lensing galaxy is barely detected and does not yield a reliable effective radius.

The system SDSS J1330+1810 was eliminated because X-ray fluxes have not been measured.

Of the original 15 systems studied by Blackburne et al. (2011), 10 systems remain in the sample.

3.2. X-Ray Fluxes

X-ray fluxes and errors were taken, for all but two cases, from Pooley et al. (2007), who chose from among multiple epochs based on signal to noise. For the two subsequently observed systems, we used the X-ray fluxes and errors given by Blackburne et al. (2011). These selection criteria ought not to bias the results derived here. The dates and identification numbers for *Chandra* observations are given in Table 3. Fluxes for the individual images are given in Table 4.

3.3. Effective Radii

The largest homogeneous source of effective radii for our quasar lenses is a series of papers that use Magain et al.'s (1998; henceforth MCS) algorithm (Claeskens et al. 2006; Eigenbrod et al. 2006; Vuissoz et al. 2008; Chantry et al. 2010; Courbin et al. 2011; Sluse et al. 2012a). The second largest is the series by Kochanek and collaborators (Kochanek et al. 2000, 2006; Morgan et al. 2006) which uses a program called `imfitfits` (Lehar et al. 2000).

Measurements using the two methods are given in Table 5. There are five systems in common. The MCS values are consistently larger than the `imfitfits` values by a factor of 1.62 (computed by averaging logarithms of ratios). It would appear that `imfitfits` systematically underestimates the effective radii, or that the MCS method systematically overestimates the effective radii, or perhaps both. We have found no persuasive reason to prefer one over the other. We have therefore taken a "split-the-difference" approach, adopting the geometric mean when we have measurements with both methods. Where we have only an `imfitfits` measurement we multiply by $\sqrt{1.62}$ and where we have only an MCS measurement we divide by $\sqrt{1.62}$.

For the one case in which we have independent measurement, that of SDSS J0924+0219, we adopt the effective radius measurement of Keeton et al. (2006), who describe a method much like that used in the SLACS survey. For HE 0230−2130, we present newly determined effective radii (P. L. Schechter et al. in preparation) and ellipticities and position angles measured with `GALFIT` (Peng et al. 2002) from images obtained at the Magellan Clay telescope.

The SLACS effective radii were obtained from fits of an elliptical de Vaucouleurs profile to a masked image of the lensing galaxy (Bolton et al. 2008). The SL2S effective radii were computed using `GALFIT`. Since we are interested in calibrating stellar mass fundamental planes obtained from these surveys, it behooves us to check whether our adopted effective radii are consistent with these.

In Figure 1 we plot the adopted effective radii against proxy velocity dispersions computed from Einstein ring radii (see Sections 2.2 and 4.2) for the present sample (filled circles) and for the SLACS sample (open circles). There is considerable overlap but considerable scatter. The overlap might be somewhat

Table 3
X-Ray Observations of Lensed Quasars

Object	Date	ObsID	Object	Date	ObsID
HE 0230−2130	2000 Oct 14	1642	MG J0414+0534	2002 Jan 9	3419
HE 0435−1223	2006 Dec 17	7761	RX J0911+0551	1999 Nov 3	419
SDSS J0924+0219	2005 Feb 24	5604	PG 1115+080	2000 Jun 3	363
RX J1131−1231	2004 Apr 12	4814	SDSS J1138+0314	2007 Feb 13	7759
B1422+231	2004 Dec 2	4939	WFI J2033−4723	2005 Mar 10	5603

Table 4
Lens System Components: Relative Positions, Convergences, Shears, Macromodel, and Observed Relative X-Ray Fluxes

Object	Component[a]	$x(''$)	$y(''$)	κ	γ	$f_{\rm mod}$[b]	f_X[b]	σ_{f_X}
HE 0230−2130	g1	−0.072	1.085					
	g2	+0.212	2.059					
	a(HM)	0.000	0.000	0.472	0.416	1.91	1.58	0.2
	b(HS)	−0.698	0.256	0.510	0.587	1.93	0.70	0.13
	c(LM)	−1.198	1.828	0.440	0.334	1.00	1.00	0.15
	d(LM)	+0.244	1.624	1.070	0.864	0.27	0.45	0.08
MG J0414+0534	g	−0.472	−1.277					
	a1(HM)	0.600	−1.942	0.489	0.454	3.48	2.13	0.1
	a2(HS)	0.732	−1.549	0.530	0.524	3.57	1.30	0.1
	b(LM)	0.000	0.000	0.460	0.316	1.00	1.00	0.05
	c(LM)	−1.342	−1.650	0.676	0.693	0.51	0.42	0.02
HE 0435−1223	g	−1.165	−0.573					
	a(LM)	0.000	0.000	0.445	0.383	1.00	1.00	0.10
	b(HS)	−1.476	0.553	0.539	0.602	1.08	.375	.047
	c(HM)	−2.467	−0.603	0.444	0.396	1.06	.378	.047
	d(LM)	−0.939	−1.614	0.587	0.648	0.65	.363	.046
RX J0911+0551	g	−0.698	0.512					
	a(HS)	0.000	0.000	0.646	0.544	2.93	3.40	0.35
	b(HM)	0.260	0.406	0.586	0.281	5.41	1.27	0.04
	c(LM)	−0.018	0.960	0.637	0.577	2.49	0.35	0.12
	d(LM)	−2.972	0.792	0.290	0.066	1.00	1.00	0.10
SDSS J0924+0219	g	−0.182	−0.859					
	a(HM)	0.000	0.000	0.472	0.456	2.31	3.15	0.7
	b(LM)	0.061	−1.805	0.443	0.383	1.00	1.00	0.25
	c(LM)	−0.968	−0.676	0.570	0.591	0.99	0.42	0.17
	d(HS)	0.536	−0.427	0.506	0.568	2.08	0.45	0.22
PG 1115+080	g	0.381	−1.344					
	a1(HM)	1.328	−2.034	0.537	0.405	3.90	3.87	0.3
	a2(HS)	1.477	−1.576	0.556	0.500	3.72	0.62	0.13
	b(LM)	−0.341	−1.961	0.658	0.643	0.66	1.05	0.10
	c(LM)	0.000	0.000	0.472	0.287	1.00	1.00	0.10
RX J1131−1231	g	−1.444	1.706					
	a(HS)	0.588	1.120	0.494	0.562	1.73	0.22	0.025
	b(HM)	0.618	2.307	0.434	0.473	1.07	2.18	0.1
	c(LM)	0.000	0.000	0.438	0.461	1.00	1.00	0.07
	d(LM)	−2.517	1.998	0.950	1.017	0.10	0.30	0.025
SDSS J1138+0314	g	0.474	0.533					
	a(HM)	0.	0.	0.465	0.384	1.40	3.20	1.0
	b(LM)	0.103	0.979	0.578	0.673	0.71	1.00	0.4
	c(LM)	1.184	0.812	0.438	0.349	1.00	1.00	0.4
	d(HS)	0.698	−0.056	0.523	0.614	1.30	1.30	0.5
B1422+231	g	0.742	−0.656					
	a(HM)	0.385	0.317	0.380	0.473	1.62	1.74	0.10
	b(HS)	0.000	0.000	0.492	0.628	1.91	0.95	0.08
	c(LM)	−0.336	−0.750	0.365	0.378	1.00	1.00	0.10
	d(LM)	0.948	−0.802	1.980	2.110	0.08	0.10	0.01
WFI J2033−4723	g	−1.438	0.308					
	a1(HM)	−2.196	1.261	0.506	0.255	1.56	0.87	0.15
	a2(HS)	−1.482	1.376	0.665	0.643	0.92	0.96	0.2
	b(LM)	0.000	0.000	0.392	0.302	1.00	1.00	0.15
	c(LM)	−2.114	−0.277	0.700	0.735	0.62	0.64	0.11

Notes.
[a] LM, HM, LS, and HS: the less magnified (L) and more highly magnified (H) minima (M) and saddle points (S) of the light travel time surface.
[b] Model and observed fluxes and errors are relative to the less magnified minimum, LM.

greater if we adopted yet larger effective radii. We note, however, that overlap with the SLACS and SL2S relations is no guarantee that our adopted effective radii are consistent. It is possible that our lensing galaxies occupy a different part of the stellar mass fundamental plane than the SLACS and SL2S samples, with a corresponding shift in effective radii. In Section 7.4 we discuss the possible effects of a systematic error in our adopted effective radii.

3.4. Positions

Positions for the quasar images and lensing galaxies given in Table 4 are taken from Blackburne et al. (2011), with the

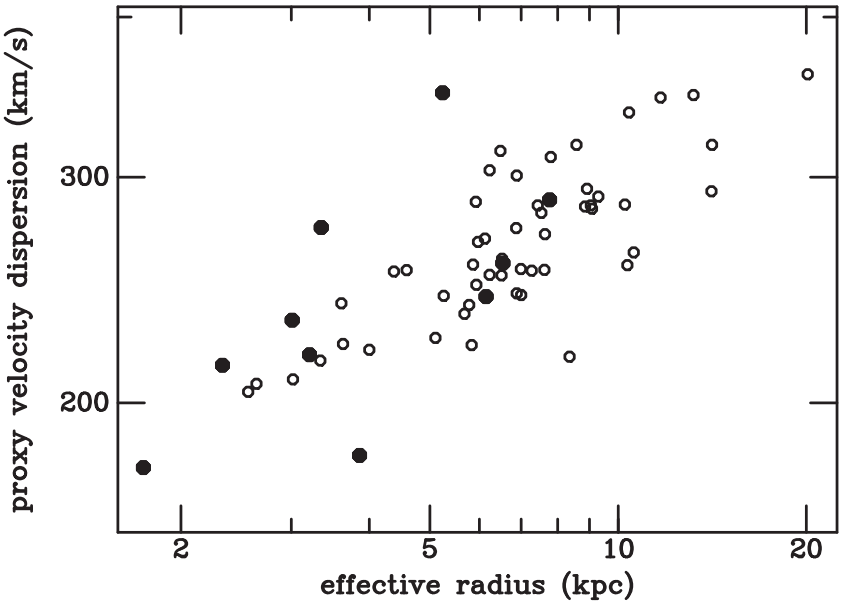

Figure 1. Proxy velocity dispersions, computed from Einstein ring radii and photometric effective radii of lensing galaxies. The filled circles are for the present sample, with proxy dispersions and the adopted effective radii taken from Table 7. The open circles are from the SLACS sample.

Table 5
Photometric Properties of Lensing Galaxies

Object (imfitfits)	$r_e(''$)	$r_e(''$) (MCS)	$r_e(''$) (adopted)	e	PA(°) (E of N)	Sources for r_e
HE 0230−2130 G1			0.51	0.34	73.0	a
HE 0230−2130 G2			0.65	0.24	−46.0	a
MG J0414+0534	0.77		0.98	0.20	84.0	b
HE 0435−1223	0.86	1.50	1.13	0.09	−1.4	c, d
RX J0911+0551	0.67	1.02	0.83	0.11	−70.0	b, e
SDSS J0924+0219	0.31	0.50	0.44	0.12	−61.3	k, f, g
PG 1115+080	0.47	0.92	0.66	0.04	−67.5	b, e
RX J1131−1231		1.51	1.19	0.25	−71.4	h
SDSS J1138+0314		0.86	0.67	0.16	−57.3	i
B1422+231	0.31	0.41	0.36	0.39	−58.9	b
WFI J2033−4723		0.61	0.48	0.18	27.8	j

Notes.
[a] P. L. Levinson et al. in preparation; [b] Kochanek et al. 2000; [c] Kochanek et al. 2006; [d] Courbin et al. 2011; [e] Sluse et al. 2012a; [f] Eigenbrod et al. 2006; [g] Keeton et al. 2006; [h] Claeskens et al. 2006; [i] Chantry et al. 2010; [j] Vuissoz et al. 2008; [k] Morgan et al. 2006.

exception of those for B1422+231, which are taken from the CASTLES gravitational lens database.[13]

3.5. Lens Galaxy Ellipticities

Ellipticities and position angles for the lensing galaxies are given in Table 4. All were taken from the compilation by Sluse et al. (2012a) in their Table B.2, with the exception of those for HE 0230−2130, which is again from P. L. Levinson et al. (in preparation).

4. MACRO-MODELS FOR LENSING POTENTIALS

Our calibration of the stellar mass fundamental plane relies on the use of micro-lensing simulations of the macro-images. The simulations, described in Section 5 below, are parameterized by a convergence, κ, a shear, γ, and a stellar contribution to the convergence, κ^*. The appropriate convergence and shear are determined from macro-models for the lensing potentials.

4.1. Singular Isothermal Ellipsoid + External Shear

In our previous work (Blackburne et al. 2011; Pooley et al. 2012), we adopted models for the gravitational potential comprised of one or more singular isothermal spheres representing lensing galaxies at their observed positions and an additional external tidal shear. We refer to these as "SIS+X" models. The choice was motivated foremost by the observation that for several of our systems there was an obvious source for the deduced external tide.

For several other systems, a model in which the quadrupole component of the potential originated in the lens, the singular isothermal ellipsoid (henceforth SIE), provided a comparably good (but not better) fit. In the interest of simplicity, Blackburne et al. (2011) adopted SIS+X models for all of the systems considered. Additional justification for this choice came from the work of Kochanek (2006), who found that external shear dominates in lensing systems.

This introduces a bias into our derived stellar mass fractions. The SIE models typically have smaller magnifications than the SIS+X models. The higher the magnification of a point source, the larger the number of micro-minima introduced by the micro-lensing stars (Granot et al. 2003). The expected fluctuations are therefore different in the two cases.

In the present study we model the potentials with both a singular isothermal ellipsoidal mass distribution *and* an external shear—SIE+X models. The ellipticity and orientation of the SIE—comprised mostly of dark matter—are not treated as free parameters, but are taken from the observed shape and orientation of the stellar component. Our SIE+X models therefore have the same number of free parameters as the Blackburne et al. (2011) SIS+X models.

The assumption that the dark halo has the same shape as the luminous stellar component is a strong one. While this is roughly consistent with previous findings (Koopmans et al. 2006), we introduced it to eliminate potential bias rather than to improve residuals from our models. But in 7 out of 10 cases,

[13] http://www.cfa.harvard.edu/castles

Table 6
Lens Model Parameters

Object	Primary Lens			Shear		Secondary Lens		
	$\theta_{\rm Ein}$	e	ϕ_e[a]	γ	ϕ_γ[a]	b_2	x_2[b]	y_2[b]
HE 0230−2130	0.″87	...	...	0.112	−59.°9	0.″33	−0.283	+0.974
MG J0414+0534	1.″11	0.20	84.0	0.063	+63.°6	0.″14	−0.385	+1.457
HE 0435−1223	1.″20	0.09	−1.40	0.063	−19.°8	...	...	...
RX J0911+0551	0.″95	0.11	−70.0	0.294	+8.°3	0.″22	−0.754	+0.665
SDSS J0924+0219	0.″87	0.12	−61.3	0.064	+66.°2	...	...	...
PG 1115+080	1.″03	...	...	...	...	2.″56	−10.883	−5.266
RX J1131−1231	1.″78	0.25	−71.4	0.068	−77.°6	...	...	...
SDSS J1138+0314	0.″67	...	...	0.098	+32.°6	...	...	...
B1422+231	0.″74	0.39	−58.9	0.137	−47.°2	...	...	...
WFI J2033−4723	1.″06	0.18	27.8	0.059	+45.°5	0.″29	+0.229	+2.020

Notes.
[a] Position angles of ellipticity, ϕ_e and external shear ϕ_γ, measured in degrees east of north.
[b] Fixed position of secondary galaxy, relative to main lensing galaxy, in arcseconds. Allowed to vary azimuthally in the case of PG 1115+080; see text. Consistent with `lensmodel` and in contrast to the entries in Table 4, the positive directions of x and y are west and north, respectively.

the residuals from the observed positions of the quasar images were substantially better for the SIE+X models than for the SIS+X models. For the three cases in which the SIE+X models gave worse fits, we use the Blackburne et al. SIS+X models. The present models are quite similar to the Blackburne et al. (2011) models, but with the macro-images slightly less strongly magnified. The systematic effect of this difference on our derived surface mass densities is discussed in Section 7.7.

Keeton's (2001) `lensmodel` program was used to obtain the model parameters that give a best fit to the observed quasar image positions. The fits were not constrained by the quasar fluxes since we expect deviations from the macro-models due to micro-lensing; these deviations are the signal we use to determine stellar masses.

The model parameters from our fits are given in Table 6. The results are very similar to those in Blackburne et al. (2011), but the systems for which we used the SIE+X model have slightly smaller magnifications. The derived convergences and shears, computed at the predicted (model) positions for the quasar images rather than those observed, are given in Table 4. The designations LM, LS, HM, and HS indicate whether the images are minima (M) or saddle points (S) of the light travel time, and whether they are more highly magnified (H) or less highly magnified (L).[14]

The model for HE 0230−2130 as two isothermals differs from that of Pooley et al. (2007), who modeled the density of the second galaxy as a power law, $\rho = \rho_0(r/r_0)^{-\gamma'}$ with an exponent $\gamma' = 1.65$. The latter gives magnifications that are larger than the former, by factors of 1.25 for images a, b, and c and 1.7 for image d. In Section 7.4 we show that use of the Pooley et al. (2007) model produces negligible change in our principal result.

But our double isothermal model produces an unobserved fifth image, a saddle point (Shin & Evans 2008), which is found where one would expect an image if the two lensing galaxies were to merge, adjusting the quadrupole to keep a, b, and c at approximately the same positions. The image should be as bright as image c and is clearly not present. While the Pooley et al. (2007) model produces no fifth image, it is *ad hoc*. Both models attribute a much smaller velocity dispersion to the second galaxy than would be warranted by its absolute magnitude. A more satisfactory model awaits measurement of mid-IR or forbidden line flux ratios, as discussed in Section 7.8.

[14] We originally adopted this notation to indicate minima and saddlepoints that were higher and lower on the light travel time surface. But in the case of HE 0230−2130, the higher saddle point is less highly magnified.

Table 7
Redshifts, Effective Radii, and Proxy Dispersions

Object	z_l	z_s	r_e (kpc)	$\sigma_{\rm prox}$ (km s^{-1})
HE 0230−2130 g1	0.523	2.163	3.21	218
g2			4.09	134
MG J0414+0534	0.96	2.64	7.77	288
HE 0435−1223	0.4541	1.689	6.54	257
RX J0911+0551	0.77	2.80	6.15	242
SDSS J0924+0219	0.39	1.524	2.33	214
PG 1115+080	0.31	1.72	3.01	232
RX J1131−1231	0.295	0.658	5.24	349
SDSS J1138+0314	0.45	2.44	3.86	182
B1422+231	0.34	3.62	1.74	178
WFI J2033−4723	0.66	1.66	3.35	274

4.2. Proxy Velocity Dispersions

Our models give Einstein ring radii measured in arcseconds. Using the lens and source redshifts, we compute the proxy velocity dispersions described in Section 2.2 that we need for our stellar mass fundamental plane. These are given in Table 7.

5. MICRO-LENSING SIMULATIONS

Our strategy is to use the stellar mass fundamental plane to predict deviations in the observed quasar X-ray fluxes from the predictions of the smooth models for the gravitational potential. As there is no closed form prediction for such fluctuations, we must simulate the observed quasar images. We use simulations carried out by Blackburne et al. (2011) using the ray-shooting technique described by Wambsganss (1990).

The Blackburne et al. (2011) simulations used the convergences and shears appropriate to the image positions in their SIS+X models, and a range of stellar contributions at each position. They populate a three dimensional model space spanned by κ, γ, and κ^*.

Our SIE+X models have somewhat different convergences and shears from the SIS+X models. But since the magnification histograms derived from these simulations vary smoothly as one varies the parameters, we have chosen to interpolate between the existing magnification histograms rather than run new simulations.

Our interpolation scheme takes advantage of the well known mass sheet degeneracy. For any triplet of convergence, κ, shear, γ, and stellar contribution to the convergence, κ^*, there is a one-dimensional locus—a line of triplets (κ', γ', $\kappa^{*\prime}$)—in the three-dimensional model space for which the magnification histogram has the identical shape but is shifted by a multiplicative factor (Paczyński 1986a; Kochanek 2004; Vernardos et al. 2014). This family is compactly parameterized by the smooth (and in our case dark) contribution to the convergence, $\kappa_s \equiv \kappa - \kappa^*$,

$$\kappa^{*\prime} = \kappa^* \left(\frac{1-\kappa_s'}{1-\kappa_s} \right), \tag{7}$$

$$\gamma' = \gamma \left(\frac{1-\kappa_s'}{1-\kappa_s} \right), \tag{8}$$

$$(1-\kappa') = (1-\kappa) \left(\frac{1-\kappa_s'}{1-\kappa_s} \right). \tag{9}$$

Projected onto the two-dimensional convergence-shear, (κ', γ'), plane, the family lies along the line connecting the point (κ, γ) to the point with unit convergence and zero shear, (1, 0).

Our lens models and those of Blackburne et al. (2011) give values for the convergences and shears (Table 4) that cluster around the line $\kappa = \gamma$, which is exactly the case for an unperturbed isothermal sphere. Our interpolation scheme is then to project all of the simulations onto the line $\kappa' = \gamma'$, with corresponding values of $\kappa^{*\prime}$. Our macro-model and the stellar mass fundamental plane gives us model values for the convergence, shear, and stellar contribution to the shear $\kappa_{\rm mod}$, $\gamma_{\rm mod}$, and $\kappa^*_{\rm mod}$. We also project these onto the $\kappa' = \gamma'$ line. We linearly interpolate between the bracketing simulations, and then linearly interpolate these between bracketing values of $\kappa^{*\prime}$. This gives us a magnification histogram appropriate to $\kappa_{\rm mod}$, $\gamma_{\rm mod}$ and $\kappa^*_{\rm mod}$.

In calibrating our stellar mass fundamental plane, we explore a wide range of multiplicative factors. There are some cases, at the extremes of this range, for which $\kappa^*_{\rm mod}$ lies outside the range of the Blackburne et al. (2011) simulations. In such cases we have used the closest simulation. All of these were at very low likelihood, and do not significantly affect our conclusions.

6. LIKELIHOOD ANALYSIS

Our goal is to obtain a "best" estimate of the factor $\mathcal{F}$ by which the surface mass density predictions from our stellar-mass fundamental plane must be multiplied to reproduce the micro-lensed X-ray fluxes observed for our quasar images.

6.1. Stellar Surface Mass Density Predictions

Given the proxy velocity dispersion $\sigma_{\rm prox}$ computed from the Einstein ring radius of the lensing galaxy and the photometric effective radius r_e of that galaxy, one can compute the predicted surface mass density at the position of the ith quasar image.

Let u_i and v_i be the position of the ith image relative to the center of the lensing galaxy, with the u and v axes aligned with the major and minor axes of the lens, respectively. For a galaxy with ellipticity e, contours of constant surface brightness lie along a locus of constant w_i, with

$$w_i^2 = (1-e)u_i^2 + v_i^2/(1-e). \tag{10}$$

The surface mass density is computed using de Vaucouleurs' (1948) law,

$$\Sigma(u_i, v_i) = \mathcal{F} \frac{\Sigma_e}{3.607} \exp\left[-\left(\frac{w_i}{r_e} \right)^{\frac{1}{4}} + 1 \right], \tag{11}$$

where Σ_e is the average surface mass density *interior* to the effective radius computed from the stellar mass fundamental plane, which, divided by 3.607, gives the surface mass density *at* the effective radius. In what follows, the dimensionless factor $\mathcal{F}$ is varied to maximize the likelihood of the observed quasar fluxes.

The stellar contribution to the dimensionless convergence, κ^*, is then given by

$$\kappa^* = \frac{4\pi G}{c^2} \frac{D_{OL} D_{LS}}{D_{OS}} \Sigma(u_i, v_i), \tag{12}$$

where D_{OL}, D_{LS}, and D_{OS} are angular diameter distances.

While several of our systems have nearby perturbing galaxies, for all but one of them the stellar surface density may be taken to come entirely from the central galaxy. The exception is HE 0230−2130, for which a second lensing galaxy lies just beyond image d. For this system we take the sum of the stellar contributions from the two galaxies.

6.2. Probability of Micro-lensed Flux

For each quasar there is an unmagnified flux that may be expressed as a magnitude, m_s. The macro-model gives macro-magnifications μ_i for each image i, computed from the convergences κ_i and shears γ_i given in Table 4,

$$\mu_i = \frac{1}{\left[(1-\kappa_i)^2 - \gamma_i^2 \right]}. \tag{13}$$

For each image, the flux expected from the macro-model, expressed as a magnitude is

$$\bar{m}_i \equiv m_s - 2.5 \log \mu_i. \tag{14}$$

Taking m_i to be the micro-lensed flux, expressed as a magnitude, for image i, a micro-lensing magnification histogram gives us the relative probability of observing an offset from the flux expected from the macro-model alone, $\mathcal{P}(m_i - \bar{m}_i | \kappa_i, \gamma_i, \kappa_i^*)$, where $\bar{m}_i$ depends upon the unmagnified flux and the macro-model for the lensing potential and where the stellar contribution to the convergence, κ_i^*, depends upon the adopted stellar mass fundamental plane, the observed proxy velocity dispersion, effective radius and ellipticity, and the scaling factor $\mathcal{F}$.

6.3. Likelihood of Unmagnified Flux

We take the likelihood $\mathcal{L}$ of the unobservable unmagnified flux, m_s, to be the probability of the micro-lensed flux for the ith image, m_i, giving us

$$\mathcal{L}(m_s | m_i, \kappa_i, \gamma_i, \kappa_i^*) = \mathcal{P}(m_i - m_s + 2.5 \log \mu_i | \kappa_i, \gamma_i, \kappa_i^*). \tag{15}$$

Note that we have implicitly assumed a uniform prior on m_s the unmagnified flux expressed as a magnitude.

For any given observation, the observed flux for the ith image, $m_{o,i}$, is comprised of the micro-lensed flux m_i plus an observational error, Δ_i. Taking the observational uncertainty in the observed X-ray flux, expressed as a magnitude, to be a Gaussian of width σ_i, and integrating over the difference Δ_i between the observed and micro-lensed fluxes, we find

$$\mathcal{L}(m_s|\kappa_i, \gamma_i, \kappa_i^*) = \int \exp\left[-\frac{\Delta_i^2}{2\sigma_i^2}\right] \times \mathcal{L}(m_s|m_{o,i} - \Delta_i, \kappa_i, \gamma_i, \kappa_i^*)d\Delta_i, \quad (16)$$

where we have ignored the small asymmetries in the flux errors. The integral has the effect of smoothing the magnification histogram.

Taking the product of the likelihoods for the four images of one of our systems, we have

$$\mathcal{L}(m_s|\mathcal{F}) = \prod_{i=1}^{i=4} \mathcal{L}[m_s|\kappa_i, \gamma_i, \kappa_i^*(\mathcal{F})], \quad (17)$$

where we now show explicitly the dependence of the four stellar contributions to the convergence, κ_i^*, on the factor $\mathcal{F}$ that calibrates the stellar mass fundamental plane.

6.4. Likelihood of the Stellar Mass Calibration Factor $\mathcal{F}$

We take the likelihood of the stellar mass calibration factor $\mathcal{F}$ to be the integral of the likelihood of the unobservable unmagnified X-ray flux,

$$\mathcal{L}_j(\mathcal{F}) = \int \mathcal{L}_j(m_{s,j}|\mathcal{F})dm_{s,j}, \quad (18)$$

where we have added the subscript j to emphasize that this is for the jth lens in our sample. Were we to place priors on the $m_{s,j}$, they would appear inside the integral on the right.

Finally, we take the product of the likelihoods for our 10 systems to give

$$\mathcal{L}(\mathcal{F}) = \prod_{j=1}^{j=10} \mathcal{L}(\mathcal{F}_j), \quad (19)$$

to give the likelihood of the calibration factor for the stellar mass fundamental plane, $\mathcal{F}$, for our complete sample.

7. THE CALIBRATION FACTOR $\mathcal{F}$ FOR THE STELLAR MASS FUNDAMENTAL PLANE

7.1. Citable Result

We have constructed the likelihood function $\mathcal{L}(F)$ for the calibration factor that multiplies our adopted stellar mass fundamental plane based on a Salpeter initial mass function using the SL2S stellar masses computed by Sonnenfeld et al. (2013).

In Figure 2 we show the relative likelihood for different values of that factor, increasing in steps of $2^{1/4}$ ($\approx$1.189). This more than doubles the sampling of our initial grid of simulations, which were carried out in steps of $10^{1/6}$ ($\approx$1.468) in stellar surface density. The median likelihood value is $\mathcal{F} = 1.23$ with a 68% confidence interval given by $0.77 < \mathcal{F} < 2.10$.

7.2. Errors in X-Ray Fluxes

We have investigated the consequences of having underestimated our errors by doubling the errors in Table 4 after first expressing them as errors in the logarithm of the flux. We find a shift in the median of $\mathcal{F}$ to a value 24% higher, which is still comfortably inside the original 68% confidence interval.

7.3. Redshift Evolution of Stellar Mass Fundamental Plane

Bezanson et al. (2013) have argued that there is relatively little evolution in the stellar mass fundamental plane with redshift. But as noted in Section 2.5, the SLACS and SL2S samples, with median redshifts of 0.205 and 0.494, respectively, give slightly different surface mass densities if one assumes the same orientation for the stellar mass fundamental plane at both redshifts. This might indicate a systematic difference between the two samples in Σ_e, r_e, or $\sigma_{\rm prox}$, or it might alternatively be taken to indicate an evolution in the calibrating factor $\mathcal{F}$. We report the result obtained using the SL2S sample because it lies much closer in redshift to the lensing galaxies in the present sample.

7.4. Systematic Errors in Lensing Galaxies' Effective Radii

As noted in Section 3.3 above, there is a systematic difference between effective radii measured using `imfitfits` and the MCS method, with the latter larger than the former by a factor of 1.62. We have used the geometric means of the two results when both were available, and multiplied the `imfitfits` results by $\sqrt{1.62}$ and divided the MCS results by $\sqrt{1.62}$ when only one was available. We have tested the effect of a systematic error in our adopted effective radii by increasing them all by a factor of $\sqrt{1.62}$. These give a calibrating factor $\mathcal{F}$ 23% smaller than our fiducial value.

We take this smaller factor to result from the fact that while the stellar mass fundamental plane gives smaller surface densities at the MCS effective radii, this is more than compensated by the fact that the quasar images are then less far out on the rapidly declining de Vaucouleurs profile.

The large differences in the measured effective radii for the lensed quasars may result from the difficulty of measuring the surface brightness profile of the lensing galaxy in the presence of four bright quasar images.

We can completely circumvent effective radius measurements by using the "fundamental line" relations obtained in Section 2.9. The lens model gives us the proxy stellar velocity dispersion $\sigma_{\rm prox}$. We then obtain effective radii from the $r_e(\sigma)$ relation and the effective surface mass density from the $\Sigma_e(\sigma)$.

The scatter from the fundamental line is somewhat larger than from the fundamental plane, and there is some danger that our sample deviates from it systematically. It is therefore reassuring to see that the median likelihood for our calibration factor $\mathcal{F}$ obtained using the fundamental line is only 7% larger than that obtained using the fundamental plane. Moreover, the likelihood distribution is, if anything, narrower.

7.5. Systematic Errors in SLACS or SL2S Effective Radii

A systematic error in either the SL2S or SLACS radii manifests itself as a shift in both the effective radii, r_e, by some factor f, and in the observed stellar surface mass densities, Σ_e. Since the effective stellar surface mass densities are obtained from total magnitudes divided by r_e^2. Such an error would drive

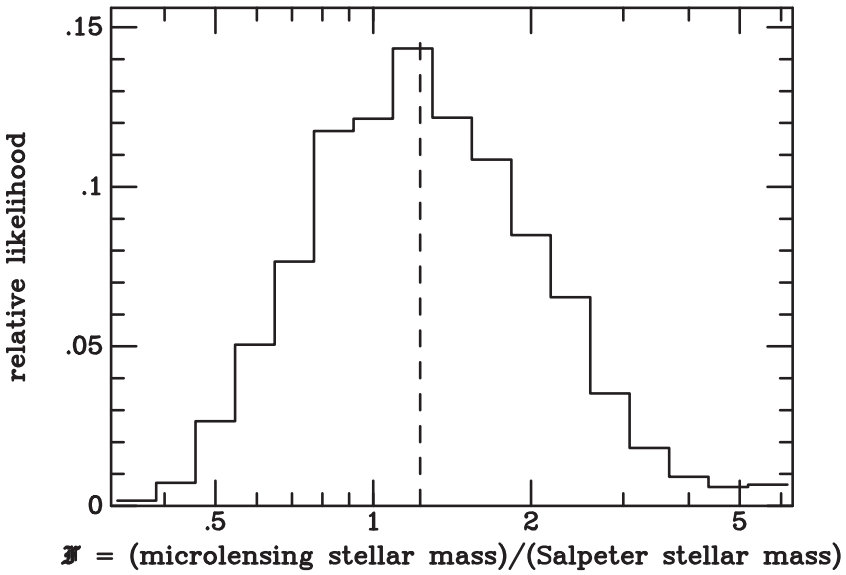

Figure 2. Likelihood of the calibration factor $\mathcal{F}$ applied to the stellar mass fundamental plane to compute the probability distribution of micro-lensing fluctuations. The dashed line shows the median likelihood value, $\mathcal{F} = 1.23$.

the constant c in the stellar mass fundamental plane down by a factor $1/f^2$. But, since $\Sigma_e \sim r_e^{-1.453}$, the net factor by which the predicted surface densities are smaller is $1/f^{0.547}$.

7.6. Effects of Mass Sheet Degeneracy

The well known mass sheet degeneracy permits the addition of a uniform surface density mass sheet to a lens model that, with corresponding adjustment of the model parameters, produces the same image positions and relative magnifications. To the extent that lensing galaxies lie in clusters of galaxies, the cluster dark matter along the line of sight to the lens acts as such a mass sheet.

In one of our lenses, PG 1115+080, we have taken this into account explicitly by modeling the associated group of galaxies as an isothermal sphere, contributing an additional convergence at the position of the lens galaxy of $\Delta\kappa = 0.105$. The convergence for an isothermal sphere is equal to the shear, so to gauge the possible effect of the mass sheet degeneracy, we might add a convergence, $\Delta\kappa$, comparable to the external shear that we measure.

Such an additional smooth contribution to the convergence does not change the magnification histogram. It does, however, increase the observed size of the Einstein ring, by a factor $(1 - \kappa)/(1 - \kappa - \Delta\kappa)$. Our proxy velocity dispersion is taken to be a property of the lensing galaxy as opposed to the galaxy plus mass sheet system. In the presence of a mass sheet we then overestimate this as well.

Our convergence values cluster around $\kappa \approx 1/2$, as expected for an isothermal sphere. The observed Einstein ring radii therefore overestimate the velocity dispersion in the galaxy by a factor $\approx(1 - 2\Delta\kappa)$. We see from Table 1 that for the same measured effective radius we will get a smaller predicted surface mass density, by a factor $\approx(1 - 2\Delta\kappa)^{1.748}$. These would lead to larger values of the calibration factor $\mathcal{F}$.

While it might seem to be more appropriate to use the smaller Einstein ring radii, we note that both the SLACS and SL2S radii were derived assuming no mass sheet. Since we seek to apply a calibrating factor to a fundamental plane derived from these data, it would seem best to use an Einstein ring radius likewise uncorrected for a possible mass sheet.

There is, however, some reason to believe (Holder & Schechter 2003) that quadruply imaged quasars experience stronger shear than the SLACS and SL2S lensing galaxies. Koopmans et al. (2006) place a limit on the external shear for a subset of the SLACS lenses of 0.035. By contrast, we see in Table 6 that the typical shear for our lensed quasars is 0.1. On the hypothesis that the external shear is the result of a larger isothermal cluster, the additional convergence would be larger for the present sample than for the SLACS sample.

The effect would not be large except for the case of RX J0911+0551, for which the lensing galaxy is clearly part of a cluster of galaxies. However, the shear, with $\gamma = 0.294$, does not seem to be directed to the center of the cluster (Kneib et al. 2000).

7.7. Systematic Errors in Lens Model and QSO Magnifications

In modeling the expected fluctuations, one must specify a convergence, κ, and a shear, γ at the positions of the quasar images. These depend upon the particular model for the gravitational lens potential. Our adopted SIE+X model is a singular isothermal ellipsoid with ellipticity and position angle taken from optical observations, with an external source of tidal shear providing as much if not more quadrupole than the SIE.

A commonly adopted alternative (and the one explicitly adopted by the SLACS and SL2S groups) is to attribute all of the quadrupole to an SIE. While there are several systems for which the SIE is manifestly inferior (there are obvious sources of tides), we have constructed SIE models for our systems and use them to gauge how large a systematic error we might be making in adopting our SIE+X models. For the SIE models we find a median likelihood value for the factor by which the Salpeter stellar mass must be multiplied which is lower by roughly 17% than for the SIE+X models.

We have also produced models with a steeper than isothermal mass density profile, $\rho(r) = \rho_0(r/r_0)^{-\gamma'}$, with exponent $\gamma' = 2.1$. The resulting calibration factor is higher by roughly 32%.

Table 8
Deviations of Radio, Mid-IR and [O III] Fluxes from Macro-model Predictions

Component	f_X	$f_{\rm mod}$	$f_{\rm mil}$	$-2.5\log(f_{\rm mil}/f_{\rm mod})$	$-2.5\log(f_X/f_{\rm mod})$
MG 0414+0534 (11.7 μ; MacLeod et al. 2013)					
HM(a1)/LM	2.13	3.56	2.96	+0.20	−0.56
HS(a2)/LM	1.30	3.88	2.74	+0.37	−1.18
LS(c)/LM	0.42	0.32	0.43	−0.36	+0.33
LM(b)/LM	≡1	≡1	≡1	≡0	≡0
PG 1115+080 (11.7 μ; Chiba et al. 2005)					
HM(a1)/LM	3.87	3.75	4.76	−0.26	+0.04
HS(a2)/LM	0.62	3.45	4.43	−0.27	−1.86
LS(b)/LM	1.05	0.78	0.76	+0.03	+0.32
LM(c)/LM	≡1	≡1	≡1	≡0	≡0
RX J1131−1231 ([O III]; Sugai et al. 2007)					
HS(a)/LM	0.22	1.77	1.37	+0.28	−2.26
HM(b)/LM	2.18	1.04	0.84	+0.23	+0.80
LS(d)/LM	0.30	0.12	...	...	+1.00
LM(c)/LM	≡1	≡1	≡1	≡0	≡0
B1422+231 (8.4 GHz; Patnaik et al. 1999)					
HM(a)/LM	1.74	1.56	1.88	−0.20	+0.12
HS(b)/LM	0.95	2.12	2.02	+0.05	−0.87
LS(d)/LM	0.10	0.06	0.06	0.00	+0.52
LM(c)/LM	≡1	≡1	≡1	≡0	≡0

7.8. Unmodeled High Order Contributions to the Lensing Potential and Milli-lensing

The macro-models for our lenses are simple as a matter of necessity: they are constrained by the positions of the quasar images but *not* the fluxes because the latter may be subject to the very micro-lensing we wish to explore—we would be running the risk of modeling out the micro-lensing. With so few constraints, we cannot allow for more than a quadrupole moment in our lensing galaxies (and at that we insist that they have the shape and orientation of the stellar component). We include the effects of visible companions and satellites but not unseen dwarf companions.

It is generally thought that the radio, mid-IR, and forbidden line emitting regions of quasars are large compared with the Einstein rings of stars and therefore not subject to micro-lensing (Mao & Schneider 1998; Chiba et al. 2005; Sugai et al. 2007; but see Sluse et al. 2013 for arguments to the contrary regarding the mid-IR). Deviations of radio, mid-IR, and forbidden line flux ratios from our models may therefore be used to gauge the contribution of unmodeled higher order components of the lensing potentials (henceforth referred to as "milli-lensing") to our X-ray flux ratio anomalies.

In Table 8 we have collected radio 8.4 GHz (Patnaik et al. 1999), mid-IR 11.7 μ (Chiba et al. 2005; MacLeod et al. 2013) and [O III] forbidden line (Sugai et al. 2007) flux ratios for four of the lenses in our sample. The remaining six lenses are as yet beyond the reach of these techniques. Likewise there is no [O III] data for the faintest image of RX J1131−1231. We did *not* include Fadely & Keeton's (2011) L' filter observations of HE 0435−1223. As they note, the degree to which the 3.8 μ emitting region is or is not subject to micro-lensing depends upon the relative contributions of the accretion disk (which is presumably micro-lensed) and dusty torus (which presumably is not) to the observed flux at that wavelength. Blackburne et al. (2011) found that the flux ratio b/a steadily increases toward unity going from the optical to the K_s filter at 2 μ. Fadely and Keeton find that b/a decreases away from unity going from 2 μ to 3.8 μ. The lens redshift is $z = 1.689$ and the emitted wavelengths are therefore correspondingly shorter.

As in Table 4, the fluxes in Table 8 are given relative to the less-magnified minimum, which is, in most cases, less likely to be affected by micro-lensing. We give the ratios (expressed as magnitude differences) of the observed to the macro-model fluxes for both the X-ray and alternative data. The former is presumably affected by both micro-lensing and milli-lensing; the latter only by milli-lensing.

We note first that the radio, mid-IR, and forbidden line fluxes are very much closer to the macro-model predictions than the X-ray fluxes. The typical milli-lensing deviation is ∼0.25 mag. The X-ray deviations are several times larger, with no obvious correlation in sign. These X-ray deviations are the signal that permits our calibration of the stellar mass fundamental plane. The milli-lensing contribution is evidently small.

The first order effect of milli-lensing would be a shift of the predicted micro-lensing distribution to brighter or fainter fluxes. Second order effects would change the shape of that distribution. The first order effect of milli-lensing would therefore seem to be the same as that of measurement errors in the X-ray fluxes.

To allow for the failure to model milli-lensing, we have analyzed our data but increased the effective uncertainties in our X-ray fluxes by adding an error of 0.25 mag in quadrature to the purely observational uncertainties. The result is to increase $\mathcal{F}$ by roughly 5%.

But rather than just allow for unknown random uncertainties, we can, for the four systems for which we have radio, mid-IR, and forbidden line data, correct the macro-lens model fluxes by the observed deviations from those models. The corrected model constrains the quantity $1/[(1-\kappa)^2-\gamma^2]$ at each image position but does not constrain separately the convergence κ and shear γ. We therefore use the uncorrected convergence and shear to generate the micro-lensing distribution (as in our uncorrected calculation) but shift it by the amount indicated by the appropriate radio, mid-IR or forbidden line observations,

for those systems for which they are available. For those without such observations, we increase the uncertainties by 0.25 mag as above. The result is to increase $\mathcal{F}$ by roughly 6%, and interestingly, to narrow the 68% confidence interval by roughly 25%

There is one case, that of HE 0230−2130, where our model has a glaring shortcoming, as described in Section 4.1. If we adopt as an alternative the model of Pooley et al. (2007), the calibration factor $\mathcal{F}$ is smaller by 1%.

7.9. Variation in the IMF with Velocity Dispersion

There is both spectroscopic and dynamical evidence that the IMF varies systematically with stellar velocity dispersion.

Spectroscopic evidence for an increasingly bottom-heavy IMF with increasing velocity dispersion has been presented by van Dokkum & Conroy (2012), La Barbera et al. (2013), and Spiniello et al. (2014). These can be used to compute stellar masses, but only if one makes the assumption about the low-mass cutoff in the IMF (Conroy & van Dokkum 2012). Spiniello et al. find an IMF slope consistent with a Chabrier IMF at a dispersion of 145 km s^{-1}, rising to a Salpeter IMF slope at a dispersion of 240 km s^{-1}.

Dynamical evidence for an increase in the ratio of stellar mass to that computed from a Salpeter IMF (again with the assumption of a stellar mass cutoff) has been presented by Treu et al. (2010), Cappellari et al. (2012), and Conroy et al. (2013). Smith (2014) has argued against the interpretation of the spectroscopic data as the effect of velocity dispersion but accepts the dynamical argument.

The mean proxy velocity dispersion for our sample is 243 km s^{-1}, with dispersions for the primary effective lensing galaxy ranging from 178 km s^{-1} to 349 km s^{-1}. One might adjust the stellar mass fundamental plane to take variations in the IMF into account, but our range in dispersion is too small, our tool too blunt, and our sample (for the present) too small to confirm such a trend.

7.10. Variation in the IMF with Radius

There is both direct and indirect evidence that the IMF might vary with radius. Martín-Navarro et al. (2014) find that for massive early-type galaxies the IMF is more bottom-heavy toward the center than further out. This is consistent with the observation that stellar abundances within a galaxy vary with escape velocity (Franx & Illingworth 1990) combined with the dependence of the IMF on stellar velocity dispersion discussed in the previous subsection.

To first approximation one might take both the stellar mass and the stellar light to be given by de Vaucouleurs profiles, with the mass having a smaller effective radius $r_{e,M}$ than that of the light, $r_{e,L}$. Using the stellar mass fundamental plane the inferred average stellar surface mass density interior to $r_{e,L}$ will have been underestimated, since more than half of the stellar mass will be interior to this radius. But the local surface mass density at $r_{e,L}$ will be a smaller fraction of this average interior density, since at the effective radius the de Vaucouleurs profile is rapidly decreasing.

Our Einstein ring radii are ∼1.5 times larger than the effective radii. If $r_{e,M} < r_{e,L}$, the predicted local surface mass density will have decreased by a larger factor from $r_{e,L}$ than we have computed using Equation (11), leading to a larger calibration factor $\mathcal{F}$.

7.11. Prior on Unmagnified X-Ray Fluxes

Implicit in our likelihood approach is the assumption that all logarithmic values for the unobservable unmagnified X-ray flux of our sources (m_s when expressed in magnitudes) are equally likely. In a Euclidean universe one would expect the numbers to increase toward fainter fluxes as $10^{0.6m_s}$. For optically selected quasars the numbers first increase more rapidly than $10^{0.6m_s}$, reflecting the increasing number density of quasars with increasing redshift, and then more slowly, reflecting a flattening or decline in the quasar number density at redshifts $z > 3$ and the dominance of relativistic effects.

Lehmer et al. (2012), in their Figure 9, show numbers of quasars with $1 < z < 3$ increasing at roughly $10^{0.3m_s}$ in the 0.5–2.0 keV band for fluxes $6 \times 10^{-16} < S < 4 \times 10^{-15}$, which we take to be the relevant range of unmagnified fluxes for our systems.

As a crude gauge of the effects of selection, we have investigated the effect of a modest prior toward fainter fluxes, $10^{0.3m_s}$. It produces an 11% shift toward a lower calibration factor $\mathcal{F}$.

7.12. Effects of Time Delay

Our likelihood analysis involves the implicit assumption that the unobservable unmagnified X-ray flux is the same for all four images. The photons that we observe were emitted at different times, spanning several weeks for most of our systems, but with differences as large as ≈150 days for the case of RX J0911+0551 (Hjorth et al. 2002). The source may have varied during this time.

The data on X-ray quasar variability is limited. Quoting from the abstract of Gibson & Brandt (2012, p. 1), "Assuming that the distribution of fractional deviations is Gaussian, its standard deviation is ≈16% on $\gtrsim$1 week timescales,..... extreme variations (>100%) are quite rare, while variation at the 25% level occurs in less that 25% of observations."

Some of the best data on X-ray quasar variability comes from lensed systems. Zimmer et al. (2011) have studied Q2237+0305, which *does* seem to have shown substantial, factor of three variation on a timescale of ≈60 days.

The multiple epoch data for MG J0414+0534, PG 1115+080, RX J1131−1231 and B1422+231 in Table 1 of Pooley et al. (2012) shows only modest evidence for coherent variation in the X-ray flux quartets, with substantially larger variations due to micro-lensing.

For the most part, the amplitude of the variability is small both with respect to our observational errors and second with respect to the width of the micro-lensing histograms, and as such seems unlikely to influence our results.

7.13. Differential Absorption by Intervening Matter

We have investigated the effects of X-ray absorption using the XSPEC spectral fitting package (Arnaud 1996). For a $z = 2$ quasar with an X-ray power-law index of 1.7 and a lens at $z = 0.5$, a factor of two reduction in the observed 0.5–8 keV band flux requires a column density of 10^{23} cm^{-2} (assuming solar abundances) in the lensing galaxy. Using the standard dust-to-gas ratio ($N_H/A_V = 1.79 \times 10^{21}$ cm^{-2} mag^{-1}), this corresponds to 55 mag of attenuation in the observed V filter (Predehl & Schmitt 1995). The absence of strong differential reddening at optical wavelengths argues against absorption as a contributor to the X-ray flux ratio anomalies.

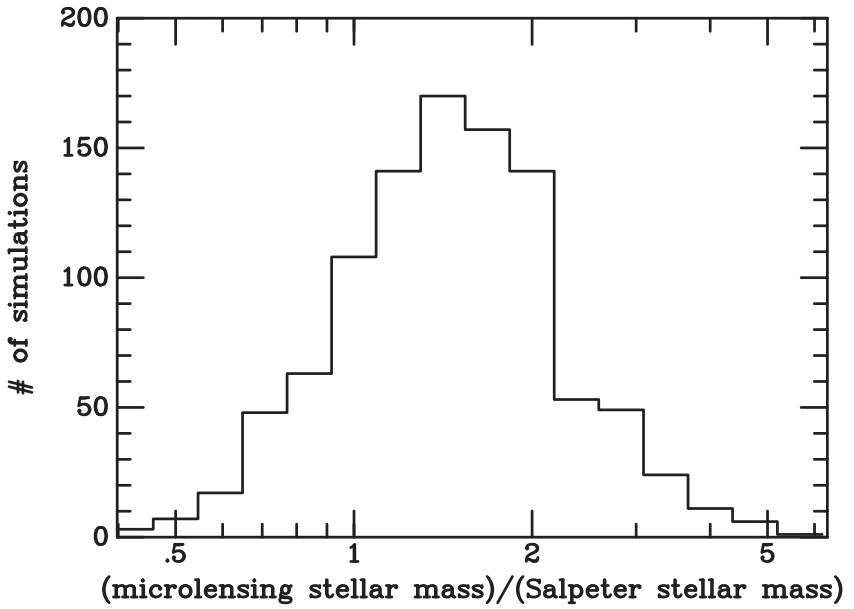

Figure 3. Results of 999 simulations of our 10 lensed systems, adopting a value of 1.414 for the calibration factor $\mathcal{F}$ that multiplies the stellar mass fundamental plane. The bars give the numbers of simulations returning median likelihood values of $\mathcal{F}$ in the ranges shown.

7.14. Consistency Check on Likelihood Analysis

As a check on the consistency of our approach, we have generated synthetic X-ray observations using our models for the lens systems and a mass surface density $\sqrt{2}$ times that for a Salpeter mass function. We assign the observed fractional error in the less magnified minimum image, taken from Table 4, to the simulated flux for that minimum. Since the less magnified minimum usually has the narrowest magnification histogram, we expect the least variation in its flux. We use this to assign errors to the remaining simulated fluxes assuming counting statistics.

We simulated each system 999 times. For each of our 999 experiments, we compute the maximum likelihood value for the derived multiplicative factor $\mathcal{F}$. A histogram is shown in Figure 3. The median maximum likelihood value is 1.530, 8% higher than the input value. The range of values including 68% of the experiments runs from 1.01 to 2.49, consistent with the width of the likelihood function for the present data.

7.15. Effects of Individual Systems on Results

We have examined the effects of the individual systems and find that one system, RX J0911+0551, has a particularly strong influence on the final result. If we exclude it from the analysis the calibration factor $\mathcal{F}$ is smaller by a factor of 1.57.

The pull of RX J0911+0551 on our principal result manifests itself in many of the above tests. For example, the effect of a change in the power law index is much smaller when RX J0911+0551 is eliminated from the sample.

There are several arguments for excluding the system. First, the integrated likelihood for the system is more than a factor of 10 smaller than the system with the next smallest likelihood. Second, we carried out a second set of 999 simulations of RX J0911+0551 with an input calibration factor $\mathcal{F} = 1.189$. In only 2.5% of the cases simulated was the likelihood of the input value smaller than that computed using the observed X-ray flux ratios. Third, at 150 days, the time delay between the d image and the other three images is the longest for any of the systems in the sample, rendering it more vulnerable to intrinsic X-ray variability.

The low likelihood for the present observations is explained by the fact that the ratio observed for the flux of image b to that of image d is 1.27, very much smaller than the 5.40 predicted by the lens model. A crude reduction of STIS spectra obtained as part of HST program GO-9854 shows a C III] line strength ratio of 3.70, roughly consistent with the lens model, as would be expected if the broad line region is comparable to or larger in size than the Einstein rings of the individual stars.

While intrinsic X-ray variability is an attractive explanation, there is nothing in the optical light curves presented by Hjorth et al. (2002) to suggest a dramatic change in either image b or image d. Our X-ray observations were obtained on JD 2451485. If intrinsic X-ray variation were to explain our unlikely result, then image d must have gotten substantially fainter in the previous 150 days, and b must have gotten substantially fainter in the subsequent 150 days. The Hjorth et al. (2002) light curves show them both getting fainter by roughly 0.1 mag, very much less than would be needed to explain our unlikely flux ratio. The intrinsic variation at X-ray wavelengths would need to be a factor of 10 larger than at optical wavelengths for this to have produced our result.

Image d lies very far from the lensing galaxy and is a minimum of the light travel time. We therefore expect it to suffer very little micro-lensing. Image b lies closer to the lensing galaxy, but as it is also a minimum, the micro-lensing distribution function lacks the tail toward fainter images that a similarly magnified saddle point image would have. The histogram is broadened, however, for higher stellar densities, making those more likely and driving up the calibration factor $\mathcal{F}$.

The above arguments constitute a rationalization for ignoring RX J0911+0551 rather than a reason.

A toy model helps make the case for the inclusion of RX J0911+0551 in our result. We suppose we have 10 systems, all of which have Gaussian likelihood distributions with the same standard deviation σ. The uncertainty in the mean will be $\sigma/\sqrt{10-1}$, or $\sigma/3$. The fact that 2.5% of our

simulated systems have likelihoods smaller than that of RX J0911+0511 would mean, under the Gaussian hypothesis, that RX J0911+0511 deviates from the true value by roughly 2.25σ. A single 2.25σ point will pull the mean of 10 objects 0.225σ, about 2/3 of the uncertainty in the mean. This is roughly what RX J0911+0511 does to the median likelihood for our 10 systems.

7.16. Cumulative Effect of Systematic Errors

In Section 7.1 we give a statistical confidence interval for our result. In the subsequent subsections, we consider a variety of systematic effects that might be thought to affect our result. Their cumulative effect might be gauged by first making a best estimate of the range and probability distribution of values within that range for the parameter that controls each systematic effect, and then choosing values for each parameter at random, reanalyzing the data, and accumulating a likelihood distribution.

We have instead made crude guesses of a plausible value for each parameter and carried out a single analysis with that parameter. If those rough guesses were correct, the largest sources of systematic error would be, in descending order, a systematic error in the exponent of our power law model for the total surface mass density (32%), a systematic error in the uncertainties in our X-ray fluxes (24%), and a systematic error in our adopted measurements of effective radii for the lensing galaxies (23%), These are still relatively small compared with our statistical uncertainty. At such time as the number of systems analyzed increases and the statistical uncertainty decreases, one will want to analyze these systematic effects more carefully.

We note that in several cases, in particular that of the power-law exponent, RX J0911+0551 plays the dominant role in determining the size of the systematic effect. One reasonably expect that with a larger sample size these systematic errors might also decrease.

8. DISCUSSION

8.1. The Dark Matter Fraction of a Typical Galaxy

We have used the stellar mass fundamental plane to combine results from the 10 lensing galaxies in our sample, since the likelihood distribution for the stellar mass surface density for any single system is quite broad. The single parameter that we constrain in this process is a calibrating factor $\mathcal{F}$ for photometrically derived stellar masses.

Previous investigators, ourselves included, have instead focused on the dark matter fraction. Our calibrated stellar mass fundamental plane can be used to derive a projected dark matter fraction as a function of r/r_e for a specific choice of $\sigma_{\rm prox}$ and r_e, making the comparison with previous work more straightforward.

In constructing our fundamental plane, we chose a fiducial galaxy with $\sigma_{\rm prox} = 266\,{\rm km\,s^{-1}}$ and $r_e = 6.17\,{\rm kpc}$. The stellar surface mass density at the effective radius, Σ_e, for such a galaxy is then $c\mathcal{F}/3.607$, or $5.04\times10^8\ M_\odot\ {\rm kpc}^{-2}$ using the SL2S result for the constant c in Table 1.

By assumption our galaxies have singular isothermal ellipsoidal mass distributions with the same ellipticity as the observed light, so that the stellar mass and dark matter fractions depend only upon the ratio of the circularized radial coordinate w defined by Equation (10) to the effective radius. The projected dark matter fraction at the effective radius for our fiducial galaxy is 62%.

In Figure 4 we show the stellar mass fraction as a function of w/r_e. The stellar mass fraction reaches a maximum at $w/r_e = 0.074$, the point at which the derivative of the de Vaucouleurs surface brightness profile is equal to that of the projected isothermal sphere. The maximum stellar mass fraction of 110% indicates the breakdown of one or more of our model assumptions: the isothermal profile for the combined mass, the de Vaucouleurs profile for the stellar mass, or the invariance with radius of the IMF (Martín-Navarro et al. 2014). But the breakdown is far inside the effective radius, affecting of the order of 10% of the mass inside the Einstein radius, and ought not have a substantial effect on our principal result.

8.2. Comparison with Previous Micro-lensing Results

The system Q2237+0305, "Huchra's Lens," has been studied by Kochanek (2004), who computes relative likelihoods for the stellar mass contribution of the convergence on a coarse grid and finds it five times as likely that κ^*/κ is unity as opposed to 0.5, implying a stellar fraction close to 100%.

This system is quite unlike the systems considered here: with a lens redshift of 0.04 the Einstein ring projects to a radius of only several hundred parsecs on the galaxy, where one might expect most of the mass to be in the form of stars. Moreover the system is a barred spiral, not an elliptical. The Kochanek result, while broad, is nonetheless consistent with our curve in Figure 4.

A second consequence of the low redshift of the lens is that the Einstein rings of individual stars project to a larger scale on the background quasar. As a result, even the optical emission region can be treated as a point source. Additionally, the velocities of stars within the lens project to much larger velocities at the redshift of the quasar. The timescale for variation is therefore much shorter than for the systems in the present sample.

Using optical data, Bate et al. (2011) have determined projected smooth (dark) matter fractions for the systems Q2237+0305, MG 0414+534, and SDSS J0924+0219. The limits for the first two of these are quite broad, but for SDSS J0924+0219 they obtain a projected smooth (dark) matter fraction at the Einstein ring, $\approx 1.97 r_e$ of $80 \pm 10\%$. The dark matter fraction at this radius for our fiducial lens is found from Figure 4 to be 82%. The prediction for a Salpeter IMF stellar mass fundamental plane can be found by dividing the stellar fraction in Figure 4 by our calibration factor $\mathcal{F} = 1.229$, yielding a dark matter fraction of 85%. The predictions for a lens with a proxy dispersion of $214\,{\rm km\,s^{-1}}$ and an effective radius of 6.94 kpc are, by coincidence, identical to those for our fiducial lens. The Bate et al. (2011) results for SDSS J0924+0219 are therefore consistent both with a Salpeter IMF and with our calibrated Salpeter IMF.

Where we use the stellar mass fundamental plane to predict the dark matter fraction at the Einstein ring, Bate et al. (2011) use a different scheme that they find underpredicts the smooth (dark matter) fraction. They start with the Bernardi et al. (2003) relation between surface brightness and effective radius (the Kormendy relation) and convert from light to mass using the Kauffmann et al. (2003) relation between stellar mass to light ratio and absolute magnitude. Kauffmann et al. (2003) use a Kroupa stellar mass function. A Salpeter IMF would have predicted yet smaller smooth mass surface densities. The fundamental plane gives better predictions of surface brightness than the Kormendy relation by virtue of using both effective radius *and* velocity dispersion, so we should not be surprised

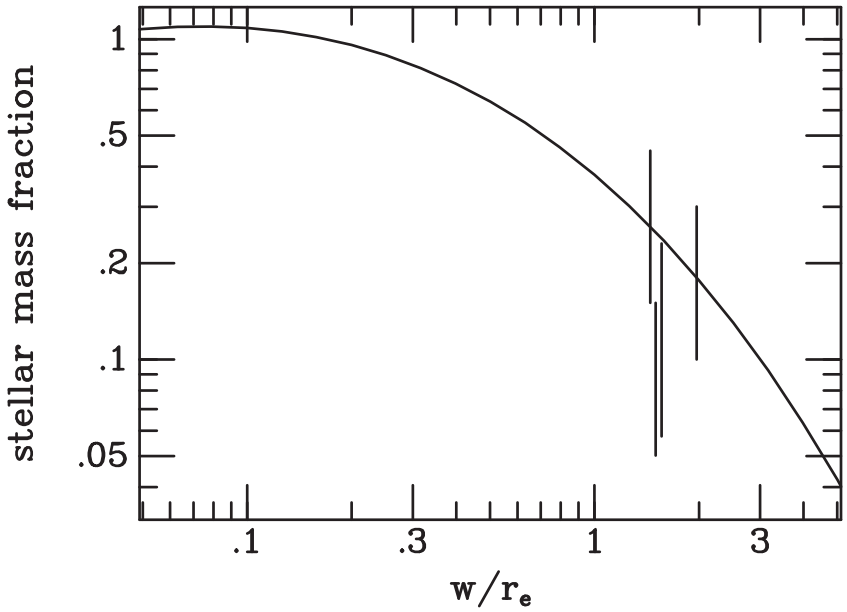

Figure 4. Stellar surface mass density as a fraction of the total for our fiducial galaxy, obtained by applying our calibration factor $\mathcal{F}$ to the stellar mass fundamental plane derived from the SLACS + SL2S samples. From left to right, the vertical bars show the 1σ confidence intervals for the stellar mass fractions for RX J1131−1231 (Dai et al. 2010), the Mediavilla et al. (2009) sample of 29 image pairs, PG 1115+080 (Morgan et al. 2008), and SDSS 0924+0219 (Bate et al. 2011).

that the dark matter fraction predicted in Section 8.1 is closer to what Bate et al. (2011) observed.

Morgan et al. (2008) carry out a joint X-ray and optical analysis of multi-epoch data for PG 1115+080. They parameterize their result by the stellar contribution to the lensing model. For the maximum likelihood value of their parameter, they find a stellar fraction at the Einstein ring of 0.115, with an uncertainty of roughly a factor of two in either direction. Using our adopted value for the effective radius, we find $\theta_{\rm Ein}/\theta_e = 1.56$. For the fiducial galaxy in Figure 4 we find a stellar fraction of 0.23. Using the measured r_e and $\sigma_{\rm prox}$ we find a stellar fraction of 0.33.

But had we adopted the `imfitfits` measurement of the effective radius ($r_e = 4.22$ kpc), which is what Morgan et al. (2008) used, we would have $\theta_{\rm Ein}/\theta_e = 2.19$, for which our fiducial galaxy would give us a stellar fraction of 15%. Using the `imfitfits` measured values $r_e = 4.22$ kpc and $\sigma_{\rm prox} = 232\,{\rm km\,s^{-1}}$, we find a stellar fraction of 18%, which would appear to be consistent with the Morgan et al. (2008) result.

Dai et al. (2010) carry out a joint X-ray and optical analysis of multi-epoch data for RX J1131−1231. They allow explicitly for errors in the model magnifications. Under their less conservative priors they find a stellar contribution to the convergence of 30% at 1.50 r_e. This is consistent with the prediction of 26% for our fiducial galaxy. Using instead the observed effective radius of 5.24 kpc and a proxy dispersion of $349\,{\rm km\,s^{-1}}$, we find again a 26% prediction for the stellar component.

Mediavilla et al. (2009) have carried out an analysis of optical flux ratios for 29 pairs of images of 20 lensed quasars. When they allow for a finite source size of 1.2×10^{16} cm, consistent with Pooley et al. (2007), they find (their Figure 8) a stellar mass fraction of 0.10 with an uncertainty of roughly 0.05. This is twice as large as when they allow for a source only half as large. For the latter case, when they allow for errors of 0.2 mag in their magnitude differences, they again find a stellar mass fraction of 0.10. They do not present results assuming both magnitude errors and the larger source size.

Mediavilla et al. (2009) compare optical continuum flux ratios to emission line ratios, mostly broad line. Sluse et al. (2012b) have argued that broad lines are micro-lensed, in which case the use of broad-line flux ratios rather than model fluxes will reduce the inferred effect of micro-lensing.

The majority of quasars in the Mediavilla sample are doubly imaged, for which the images are more broadly scattered to radii larger and smaller than the Einstein radius. They do not give effective radii, but for $\theta_{\rm Ein}/\theta_e \sim 1.5$, as is typical of our sample, we would predict substantially larger stellar mass fractions of $\sim$0.25.

The present work includes two substantial refinements over the Mediavilla et al. (2009) effort. First, we parameterize by mass-to-light ratio rather than by stellar fraction, thereby allowing for a range of impact parameters and effective radii (and thus a range in stellar mass fractions). Second we use X-ray flux ratios, on the hypothesis that the X-ray emitting regions are point-like.

Oguri et al. (2014) have carried out an analysis that has multiple points in common with the present analysis. They work with a sample of strong lenses, including the lensed galaxies in the SLACS, SL2S, and BELLS (Brownstein et al. 2012) samples and also 28 of the lensed quasars in the CASTLES database. They compute stellar masses from the photometry and calculate dynamical masses interior to the Einstein ring. They add a power law dark matter halo to bring the two into agreement. They parameterize the stellar contribution with a parameter $\alpha^{\rm Sal}_{\rm SPS}$, which gives the ratio of the stellar contribution to that computed from a Salpeter IMF, and which is essentially our calibration factor $\mathcal{F}$. They parameterize the dark matter contribution by A_{DM} which gives the ratio of the projected dark matter contribution within the effective radius to the total stellar mass. These parameters are strongly degenerate.

Oguri et al. use the dark matter fraction likelihood distributions for 12 quasars given by the present authors (Pooley et al. 2012) and three given by Bate et al. (2011) to break this degeneracy. They add an additional parameter, γ'_{DM}, the slope of the density power law adopted for the dark matter halo, which they also allow to vary. They find $\alpha_{\rm SPS}^{\rm Sal} = 0.92^{+0.09}_{-0.08}$.

A particularly intriguing feature of this result is that the fractional uncertainty in $\alpha_{\rm SPS}^{\rm Sal}$ is smaller by a factor of five than the width of the likelihood for the stellar fraction given in Pooley et al. (2012) and likewise that of the present result for $\mathcal{F}$. Figures 3 and 4 of Oguri et al. show a broad range of allowed values for $\alpha_{\rm SPS}^{\rm Sal}$ in the absence of the micro-lensing constraints. An additional micro-lensing constraint with an uncertainty of a factor of 1.5 in $\alpha_{\rm SPS}^{\rm Sal}$ would not seem sufficient to narrow the allowed values to the claimed range of only 10%.

Oguri et al. favor a power-law exponent for the total mass density, $\rho = \rho_0(r/r_0)^{-\gamma'}$, of $\gamma' = 2.11$, slightly steeper than the isothermal assumed here. As noted in Section 7.7, using a power law this steep would increase our calibration factor $\mathcal{F}$ by roughly 32%, increasing the disagreement with the Oguri et al. result.

Mediavilla et al. (2009), Bate et al. (2011), and Pooley et al. (2012) all parameterized their results by a single dark matter fraction for all four images. In the present effort, we have taken explicit account of the differing distances of the quasar images from their host galaxies, and of the ellipticity of the underlying light distribution. The micro-lensing histograms are often quite different for images that are saddle points and minima. The minima tend to lie further from the lensing galaxy, and therefore have lower stellar surface densities than saddle points. Moreover, to the extent that the ellipticity of the light is aligned with the potential, the minima will tend to lie along the stellar minor axis, producing yet lower stellar surface densities.

The Oguri et al. result assumes a power-law dark matter halo, where the present result assumes a power law (isothermal) for the total surface mass density. In the present analysis, the power-law index enters primarily in the computed convergences and shears. Changing that index has an effect similar to adding or subtracting a mass sheet, as described in Section 7.6, driving the present result further from the Oguri et al. result. By the same token, Pooley et al. (2012) used convergences and shears appropriate to an isothermal. Had they used $\gamma' = 2.11$, they would have deduced larger stellar mass fractions, driving the Oguri et al. results closer to the present results.

9. CONCLUSIONS AND OUTLOOK

We have determined the factor by which the stellar mass fundamental plane at $z \sim 0.5$ must be increased if the anomalies in the observed X-ray fluxes from our sample of quadruply macro-lensed quasars are attributed to micro-lensing by the stars in the lensing galaxy.

Constructing our stellar mass fundamental plane from the lensing early-type galaxies in the SLACS and SL2S surveys, using stellar masses as computed by Auger and collaborators (Auger et al. 2010; Sonnenfeld et al. 2013) assuming a Salpeter IMF, the factor by which the stellar mass fundamental plane must be scaled is $\mathcal{F} = 1.23$, with a one sigma confidence interval $0.77 < \mathcal{F} < 2.10$.

The result includes the mass due to white dwarfs, neutron stars, stellar mass black holes, brown dwarfs, and red dwarfs too faint to contribute significantly to the observed light.

We have investigated a number of possible sources of systematic error and estimated how large the effects might be.

The greatest single source of uncertainty is sample size. While this can be addressed with the discovery and followup observation of additional systems, to the extent that newly discovered systems are not as bright as those in the present sample, they will be less amenable to observations with *Chandra*. Moreover the presumptive follow-on mission to *Chandra*, Athena+, will not have the necessary angular resolution.

We note that for the systems in our sample that are faintest in the optical, SDSS J0924+0219 and SDSS J1138+0314, the optical flux ratios are nearly identical to the X-ray flux ratios. This suggests that the optical emission is coming from a region that is relatively small compared to the Einstein rings of the stars, and that X-ray fluxes may not be needed for this kind of analysis.

Beyond that there is a systematic uncertainty arising from systematic differences in the effective radii measured for our lensing galaxies. Observations with the *James Webb Space Telescope* (*JWST*) might in principle resolve these, since the point source point-spread function will be very much smaller than the image separations. More extensive photometric observations with *JWST* would permit the direct local calculation of the stellar surface mass density using an assumed IMF, circumventing the stellar mass fundamental plane.

We owe Professor Saul Rappaport a particular debt of gratitude for raising the question of what one might hope to learn from X-ray observations of lensed quasars. P.L.S. and J.A.B. acknowledge support from NSF grants AST 02-06010 and AST 06-07601 and Chandra grant GO7-8099. P.L.S. gratefully acknowledges the hospitality of Williams College during the academic year 2013–2014. D.P. gratefully acknowledges support from Chandra grants GO1-12135 and GO3-14102. J.W. acknowledges with great pleasure generous support received during his tenure as Schroedinger Visiting Professor 2013 at the Pauli Center for Theoretical Studies which is supported by the Swiss National Science Foundation (SNF), ETH Zürich, and the University of Zürich.

REFERENCES

Arnaud, K. A. 1996, in ASP Conf. Ser. 101, Astronomical Data Analysis Software and Systems V, ed. G. H. Jacoby & J. Barnes (San Francisco, CA: ASP), 17
Auger, M. W., Treu, T., Bolton, A. S., et al. 2010, ApJ, 724, 511
Bate, N. F., Floyd, D. J. E., Webster, R. L., & Wyithe, J. S. B. 2011, ApJ, 731, 71
Bernardi, M., Sheth, R. K., Annis, J., et al. 2003, AJ, 125, 1849
Bezanson, R., van Dokkum, P. G., van de Sande, J., et al. 2013, ApJL, 779, L21
Blackburne, J. A., Pooley, D., Rappaport, S., & Schechter, P. L. 2011, ApJ, 729, 34
Bolton, A. S., Brownstein, J. R., Kochanek, C. S., et al. 2012, ApJ, 757, 82
Bolton, A. S., Burles, S., Koopmans, L. V. E., et al. 2008, ApJ, 682, 964
Brownstein, J. R., Bolton, A. S., Schlegel, D. J., et al. 2012, ApJ, 744, 41
Cappellari, M., McDermid, R. M., Alatalo, K., et al. 2012, Natur, 484, 485
Chabrier, G. 2003, PASP, 115, 763
Chantry, V., Sluse, D., & Magain, P. 2010, A&A, 522, A95
Chiba, M., Minezaki, T., Kashikawa, N., Kataza, H., & Inoue, K. T. 2005, ApJ, 627, 53
Claeskens, J.-F., Sluse, D., Riaud, P., & Surdej, J. 2006, A&A, 451, 865
Conroy, C., Dutton, A. A., Graves, G. J., Mendel, J. T., & van Dokkum, P. G. 2013, ApJL, 776, L26
Conroy, C., & van Dokkum, P. G. 2012, ApJ, 760, 71
Courbin, F., Chantry, V., Revaz, Y., et al. 2011, A&A, 536, A53
Courteau, S., Cappellari, M., de Jong, R. S., et al. 2014, RvMP, 86, 47
Dai, X., Kochanek, C. S., Chartas, G., et al. 2010, ApJ, 709, 278
de Vaucouleurs, G. 1948, Comtes Rendus, 227, 548
Djorgovski, S., & Davis, M. 1987, ApJ, 313, 59
Eigenbrod, A., Courbin, F., Dye, S., et al. 2006, A&A, 451, 747

Fadely, R., & Keeton, C. R. 2011, AJ, 141, 101
Franx, M., & Illingworth, G. D. 1990, ApJL, 359, L41
Gavazzi, R., Treu, T., Rhodes, J. D., et al. 2007, ApJ, 667, 176
Gibson, R. R., & Brandt, W. N. 2012, ApJ, 746, 54
Granot, J., Schechter, P. L., & Wambsganss, J. 2003, ApJ, 583, 575
Hjorth, J., Burud, I., Jaunsen, A. O., et al. 2002, ApJL, 572, L11
Holder, G. P., & Schechter, P. L. 2003, ApJ, 589, 688
Hyde, J. B., & Bernardi, M. 2009, MNRAS, 396, 1171
Kauffmann, G., Heckman, T. M., White, S. D. M., et al. 2003, MNRAS, 341, 33
Kayser, R., Refsdal, S., & Stabell, R. 1986, A&A, 166, 36
Keeton, C. R. 2001, arXiv:astro-ph/0102340
Keeton, C. R., Burles, S., Schechter, P. L., & Wambsganss, J. 2006, ApJ, 639, 1
Kneib, J.-P., Cohen, J. G., & Hjorth, J. 2000, ApJL, 544, L35
Kochanek, C. S. 2004, ApJ, 605, 58
Kochanek, C. S. 2006, in Saas-Fee Advanced Course 33: Gravitational Lensing: Strong, Weak and Micro, ed. G. Meylan, P. Jetzer, & P. North (Berlin: Springer), 91
Kochanek, C. S., Falco, E. E., Impey, C. D., et al. 2000, ApJ, 543, 131
Kochanek, C. S., Morgan, N. D., Falco, E. E., et al. 2006, ApJ, 640, 47
Koopmans, L. V. E., Treu, T., Bolton, A. S., Burles, S., & Moustakas, L. A. 2006, ApJ, 649, 599
Kroupa, P. 2001, MNRAS, 322, 231
La Barbera, F., Ferreras, I., Vazdekis, A., et al. 2013, MNRAS, 433, 3017
Lehar, J., Falco, E. E., Kochanek, C. S., et al. 2000, ApJ, 536, 584
Lehmer, B.-D., Xue, Y.-Q., Brandt, W-N., et al. 2012, ApJ, 752, 46
MacLeod, C. L., Jones, R., Agol, E., & Kochanek, C. S. 2013, ApJ, 773, 35
Magain, P., Courbin, F., & Sohy, S. 1998, ApJ, 494, 472
Mao, S., & Schneider, P. 1998, MNRAS, 295, 587
Martín-Navarro, I., La Barbera, F., Vazdekis, A., Falcón-Barroso, J., & Ferreras, I. 2014, arXiv:1404.6533
Mediavilla, E., Muñoz, J. A., Falco, E., et al. 2009, ApJ, 706, 1451
Morgan, C. W., Kochanek, C. S., Dai, X., Morgan, N. D., & Falco, E. E. 2008, ApJ, 689, 755
Morgan, C. W., Kochanek, C. S., Morgan, N. D., & Falco, E. E. 2006, ApJ, 647, 874
Mosquera, A. M., & Kochanek, C. S. 2011, ApJ, 738, 96
Nair, P., van den Bergh, S., & Abraham, R. G. 2011, ApJL, 735, L31
Narayan, R., & Bartelmann, M. 1996, arXiv:astro-ph/9606001
Oguri, M., Rusu, C. E., & Falco, E. E. 2014, MNRAS, 439, 2494
Paczyński, B. 1986a, ApJ, 301, 503
Paczyński, B. 1986b, ApJ, 304, 1
Patnaik, A. R., Kemball, A. J., Porcas, R. W., & Garrett, M. A. 1999, MNRAS, 307, L1
Peng, C. Y., Ho, L. C., Impey, C. D., & Rix, H.-W. 2002, AJ, 124, 266
Pooley, D., Blackburne, J. A., Rappaport, S., & Schechter, P. L. 2007, ApJ, 661, 19
Pooley, D., Rappaport, S., Blackburne, J. A., Schechter, P. L., & Wambsganss, J. 2012, ApJ, 744, 111
Predehl, P., & Schmitt, J. H. M. M. 1995, A&A, 293, 889
Ruff, A. J., Gavazzi, R., Marshall, P. J., et al. 2011, ApJ, 727, 96
Salpeter, E. E. 1955, ApJ, 121, 161
Schechter, P. L., & Wambsganss, J. 2002, ApJ, 580, 685
Schechter, P. L., & Wambsganss, J. 2004, in IAU Symp. 220, Dark Matter in Galaxies, ed. S. Ryder, D. Pisano, M. Walker, & K. Freeman (Cambridge: Cambridge Univ. Press), 103
Schechter, P. L., Wambsganss, J., & Lewis, G. F. 2004, ApJ, 613, 77
Schneider, P., & Weiss, A. 1987, A&A, 171, 49
Shin, E. M., & Evans, N. W. 2008, MNRAS, 390, 505
Sluse, D., Chantry, V., Magain, P., Courbin, F., & Meylan, G. 2012a, A&A, 538, A99
Sluse, D., Hutsemékers, D., Courbin, F., Meylan, G., & Wambsganss, J. 2012b, A&A, 544, A62
Sluse, D., Kishimoto, M., Anguita, T., Wucknitz, O., & Wambsganss, J. 2013, A&A, 553, A53
Smith, R. J. 2014, MNRAS, 443, L69
Sonnenfeld, A., Gavazzi, R., Suyu, S. H., Treu, T., & Marshall, P. J. 2013, ApJ, 777, 97
Spiniello, C., Trager, S., Koopmans, L. V. E., & Conroy, C. 2014, MNRAS, 438, 1483
Sugai, H., Kawai, A., Shimono, A., et al. 2007, ApJ, 660, 1016
Treu, T., Auger, M. W., Koopmans, L. V. E., et al. 2010, ApJ, 709, 1195
van Dokkum, P. G., & Conroy, C. 2012, ApJ, 760, 70
Vernardos, G., Fluke, C. J., Bate, N. F., & Croton, D. 2014, ApJS, 211, 16
Vuissoz, C., Courbin, F., Sluse, D., et al. 2008, A&A, 488, 481
Wambsganss, J. 1990, PhD thesis, Ludwig-Maximillians-Universität at Münich
Witt, H. J., Mao, S., & Schechter, P. L. 1995, ApJ, 443, 18
Zimmer, F., Schmidt, R. W., & Wambsganss, J. 2011, MNRAS, 413, 1099